Field off Scattering Studies in Lithium Hydride

R. Bayes, J. C. Nugent & P. Soler
The MICE collaboration

Multiple coulomb scattering is a well known electromagnetic phenomenon experienced by charged particles traversing materials. However, from recent measurements by the MuScat experiment it is known that the available simulation codes, specifically GEANT4, overestimate the scattering of muons in low Z materials. This is of particular interest to the Muon Ionization Cooling Experiment (MICE) which has the goal of measuring the reduction of a muon beam emittance induced by energy loss in low Z absorbers. Multiple scattering induces positive changes in the emittance in contrast to the reduction due to ionization energy loss. It therefore is essential that MICE measures multiple scattering for its absorber materials; lithium hydride and liquid hydrogen; and validate the multiple scattering against known simulations. MICE took data with magnetic fields off suitable for multiple scattering measurements in the spring of 2016 using the lithium hydride absorber. The data was compared to a convolution between data collected with no absorber and specific models of scattering in lithium hydride, including the default GEANT4 model. A deconvolution procedure was also applied to the data to extract the scattering distribution within the absorber material. The results for the comparisons and the deconvolved scattering widths are reported for the three nominal beam momenta; 172 MeV/c, 200 MeV/c, and 240 MeV/c. A momentum dependent measurement of multiple scattering in lithium hydride was also conducted and the result was compared to muon beams used to collect the lithium hydride data allow momentum dependent measurements of the scattering to be conducted and compared with the accepted scattering model.

1 Introduction

MICE intends to make a measurement of emittance reduction in low Z absorbers such as liquid hydrogen and lithium hydride. The beam emittance is increased by the scattering in the absorber material. The change in the emittance [1] is given by

$$\frac{d\epsilon_n}{dz} \approx -\frac{\epsilon_n}{p_\mu \beta}\left\langle \frac{dE_\mu}{dz} \right\rangle + \frac{\beta_\perp p_\mu}{2m}\frac{d\Theta^2}{dz} \tag{1}$$

where Θ is the RMS scattering width, and $\frac{dE}{dz}$ is the energy loss of a muon. The normalized emittance is $\epsilon_n = \sqrt[4]{det(Var(x, y, p_x, p_y))}/m_\mu$ for a muon with a mass m_μ, a momentum p_μ, relativistic velocity $\beta = v_\mu/c$, and a transverse momentum distribution with an extent given by $\beta_\perp$. Multiple scattering has not been well modelled for low Z absorbers in standard simulations, historically speaking. Data collected by the MuScatt experiment [2] indicates that GEANT overestimates the scattering for these materials[3]. For MICE to make believable predictions of the emittance in the absorber materials the model in the simulation must be validated, or a new model must be introduced that provides a better reflection of what exists in data. This is particularly important for the prediction of the equilibrium emittance; the case when $d\epsilon_n/dz = 0$ and

$$\epsilon_n = \frac{\beta_\perp p_\mu^2 \beta}{2m}\frac{d\Theta^2}{dz}\left\langle \frac{dE_\mu}{dz} \right\rangle^{-1}. \tag{2}$$

This provides the minimum emittance for which cooling is effective.

1.1 Definitions

Multiple scattering is characterized using either the angle between the initial and final momentum vectors or the difference of angles that those vectors make when projected onto a given coordinate plane. The former is perhaps more intuitive and is expressed mathematically as

$$\theta_{Scatt} = \text{acos}\left(\frac{\mathbf{p}_{US}\cdot\mathbf{p}_{DS}}{|\mathbf{p}_{US}||\mathbf{p}_{DS}|}\right) \tag{3}$$

where $\mathbf{p}_{US}$ and $\mathbf{p}_{DS}$ are the momentum vectors measured by the upstream and downstream trackers, respectively. Alternatively the projection of the scattering angle onto the X-Z or Y-Z plane may be considered. This can be defined by considering the inner product of the downstream momentum with the component of the upstream momentum vector perpendicular to the projection plane vector. For example the scattering projection into the plane defined by the momentum vector and the y-axis should be

$$\theta_y = \text{atan}\left(\frac{\mathbf{p}_{DS}\cdot\hat{\mathbf{u}}}{\mathbf{p}_{DS}\cdot\hat{\mathbf{v}}}\right) = atan\left(\frac{\mathbf{p}_{DS}\cdot(\hat{\mathbf{y}}\times\mathbf{p}_{US})|\mathbf{p}_{US}|}{(\mathbf{p}_{DS}\cdot\mathbf{p}_{US})|\hat{\mathbf{y}}\times\mathbf{p}_{US}|}\right) \tag{4}$$

where $\hat{\mathbf{y}}$ is the unit vector in the y direction, $\hat{\mathbf{v}} = \hat{\mathbf{y}}\times\mathbf{p}_{US}/|\hat{\mathbf{y}}\times\mathbf{p}_{US}|$ is the unit vector mutually orthogonal to the y direction and the momentum vector and $\hat{\mathbf{u}} = \mathbf{p}_{US}/|\mathbf{p}_{US}|$ is the unit vector parallel to the upstream momentum vector. A scattering angle in the perpendicular plane must then be defined as

$$\theta_x = \text{atan}\left(|\mathbf{p}_{US}|\frac{\mathbf{p}_{DS}\cdot(\mathbf{p}_{US}\times(\hat{\mathbf{y}}\times\mathbf{p}_{US}))}{|\mathbf{p}_{US}\times(\hat{\mathbf{y}}\times\mathbf{p}_{US})|\mathbf{p}_{DS}\cdot\mathbf{p}_{US}}\right) \tag{5}$$

where the downstream vector is now projected onto the unit vector $\hat{\mathbf{v}} = \mathbf{p}_{US}\times(\hat{\mathbf{y}}\times\mathbf{p}_{US})/|\mathbf{p}_{US}\times(\hat{\mathbf{y}}\times\mathbf{p}_{US})|$. These two expressions can be expressed in terms of the gradients of the muon tracks before and after the scatters;

$$\theta_x = \text{atan}\left(\sqrt{\frac{1+\frac{dx}{dz}{}^2_{US}+\frac{dy}{dz}{}^2_{US}}{(1+\frac{dx}{dz}{}^2_{US}+\frac{dy}{dz}{}^2_{US})(1+\frac{dx}{dz}{}^2_{US})}}\left\{\frac{\frac{dy}{dz}_{DS}(1+\frac{dx}{dz}{}^2_{US})-(\frac{dx}{dz}_{DS}\frac{dx}{dz}_{US}-1)\frac{dy}{dz}_{US}}{1+\frac{dx}{dz}_{US}\frac{dx}{dz}_{DS}+\frac{dy}{dz}_{US}\frac{dy}{dz}_{DS}}\right\}\right) \tag{6}$$

$$\theta_y = \text{atan}\left(\frac{\sqrt{1+\frac{dx}{dz}{}^2_{US}+\frac{dy}{dz}{}^2_{US}}}{\sqrt{1+\frac{dx}{dz}{}^2_{US}}}\left\{\frac{\frac{dx}{dz}_{DS}-\frac{dx}{dz}_{US}}{1+\frac{dx}{dz}_{US}\frac{dx}{dz}_{DS}+\frac{dy}{dz}_{US}\frac{dy}{dz}_{DS}}\right\}\right) \tag{7}$$

In the approximation of small angles (i.e. $\frac{dx}{dz}\approx\frac{dy}{dz}\ll 1$) these produce the more familiar forms;

$$\theta_x = \frac{dy}{dz}_{DS} - \frac{dy}{dz}_{US} \tag{8}$$

for scattering about the x-axis or

$$\theta_y = \frac{dx}{dz}_{DS} - \frac{dx}{dz}_{US} \tag{9}$$

for scattering about the y-axis. The more exact expressions will be used for this analysis.

1.2 Scattering Predictions for MICE

The behaviour of the coulomb scattering is a material dependent quantity which has been described by the radiation length X_0. Greisen and Rossi derived an expression for the RMS scattering width that has been further developed by other authors and is expressed by the particle data group as

$$\Theta = \frac{13.6\text{ MeV/c}}{p_\mu\beta}\sqrt{\frac{z}{X_0}}\left(1+0.038\ln\frac{z}{X_0}\right). \tag{10}$$

where z is the material thickness, and X_0 is expressed in cm. The $\left(1 + 0.038 \ln \frac{z}{X_0}\right)$ term is an empirical correction for the material dependence of the expression. Equation 1 is applicable to the projections of the multiple scattering angles on the X-Z or Y-Z plane. The projected scattering angles are related to the scattering angle in space by a factor of $\sqrt{2}$, or $\Theta_X^2 + \Theta_Y^2 \approx \Theta_{Scatt}^2$. Multiple scattering produces a distribution that is Gaussian with respect to the projected scattering angles for small angles at which Eq.10 has an uncertainty of 1% for most materials.

Given Eq. 10, a prediction of the scattering width may be made for the material in the MICE channel. Comparisons with Eq. 10 are not sufficient because this scattering width is only considered valid for the central 98% of the distribution. The purpose of these measurements is to compare the scattering to that in simulation and to evaluate the distributions for all accessible angles. Geant 4[4] as part of its default physics list, uses the "Wentzel VI" model for multiple scattering at all angles for muons, pions, kaons, protons, and anti-protons at all energies. This model uses the scattering probability differential in the solid angle ω and the material thickness z.

$$\Xi(\theta) d\omega dz = 4 N_a \frac{Z^2}{A} r_e^2 \left(\frac{m_e c}{\beta p}\right)^2 \frac{d\omega}{(\theta_1^2 + \theta^2)^2} dz \tag{11}$$

for a number of atoms N_a with atomic number Z and atomic weight A given an incident particle with momentum p and $\beta = p/E$ which can then be integrated over solid angle ω to produce a rate of change of the mean square scattering angle

$$\frac{d\theta^2}{dz} = 4 N_a \frac{Z^2}{A} r_e^2 \left(\frac{m_e c}{\beta p}\right)^2 \left(\ln\left[\left(\frac{\theta_2}{\theta_1}\right) + 1\right] - 1 + \frac{1}{Z}\left(\ln\left[\left(\frac{\theta_2}{\theta_1}\right)^2 + 1\right] - 1\right)\right). \tag{12}$$

assuming that the scattering cross-section for nuclei and electrons is the same. In the above equations θ_1 and θ_2 are the integration minimum and maximum angles. GEANT uses a compact implementation[5] of the model to simulate the distribution; that is it uses a representation of the scattering distributions to replicate the scattering behaviour of particles over a given step through a material rather than simulating single interactions. The scattering distributions of muons in lithium hydride at three different momenta as predicted by GEANT are shown in Fig. 20a.

The measurement in MICE consists of looking at the residuals between the scattering in data and that predicted by the models and determining which model is the best fit to the reconstructed data. This difference is expressed using

$$\chi^2 = \sum_{i=0}^{N} \frac{(n_{data}(\theta_i^{rec}) - n_{conv.}(\theta_i^{rec}))^2}{n_{conv.}(\theta_i^{rec}) + \sum \sigma_{sys,i}^2} \tag{13}$$

where $n_{data}(\theta_i^{rec})$ is the number of events reconstructed at a reconstructed scattering angle (3D or projection angle) contained in the ith bin and $n_{conv}(\theta_i^{rec})$ is the number of events in the convolved distribution for the matching bin.

1.3 MICE Channel

Scattering in MICE may be measured across two trackers consisting of five scintillator fibre triplet planes each immersed in helium gas arranged symmetrically about a central absorber. The tracker triplet planes do not provide an independant measurement of x and y as the three planes are at 120° to each other. This allows the x-y co-ordinates of any hit to be reconstructed but the measurement is not indepentant. Despite this the measurement of mutiple scattering is made in terms of these two paramters as the MICE beam line does focus and defocus in x and y and a cross check of the definitions is included as a systematic error in section 5.4.

Table 1: Material budget affecting tracks passing through the MICE LiH absorber. The material thickness normalized by the radiation length is given with the RMS of the scattering distribution calculated using the expression from the PDG. Note that the effective thickness shown for the tracker materials (He and Scint. Fibres) is for one tracker.

				Θ (mrad)		
Material	z(cm)	z/X_0	ρ (gm^{-3})	172 MeV/c	200 MeV/c	240 MeV/c
Tracker He	113	0.00015	1.663×10^{-4}	0.8	0.6	0.5
Al Window	0.016	0.00179	2.699	3.5	2.9	2.3
Scint. Fibres	0.74	0.0175	1.032	10.4	8.6	6.9
Total				12.5	10.4	8.3
LiH	6.5	0.064	0.8200	20.7	17.2	13.8
Total wi/ LiH				25.9	21.5	17.3
Helium	22.2	2.94×10^{-5}	1.663×10^{-4}	0.30	0.25	0.20
Total wi/ He				12.5	10.4	8.4

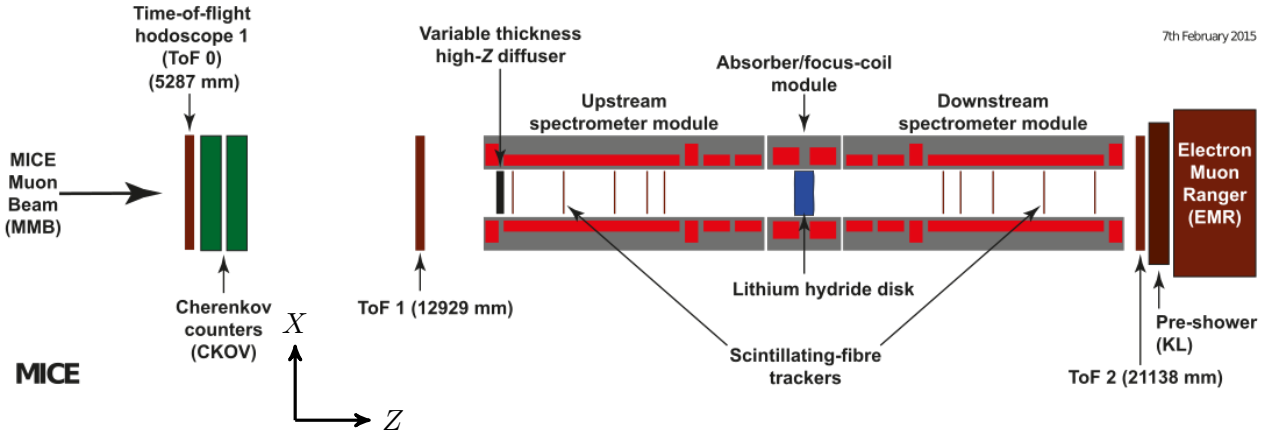

Figure 1: MICE cooling channel

Table 2: Data collected for the purpose of measuring muon scattering in MICE in February and March of 2016 listed by beam line setting.

(a) Data runs collected for field off multiple scattering

Zero Absorber			LiH Absorber					
3-172 MeV/c	3-200 MeV/c	3-240 MeV/c	3-172 MeV/c		3-200 MeV/c		3-240 MeV/c	
7666	7652	7674	7764	7826	7726	7807	7727	7817
7675	7672	7682	7766	7827	7729	7834	7733	7818
7676	7673	7685	7767	7831	7735	7835	7737	7819
7680	7681	7691	7782	7832	7736	7836	7738	7844
7683	7695	7693	7783	7861	7754	7838	7775	7847
7684		7694	7785	7863	7770	7841	7776	7848
7690			7786	7864	7771	7842	7790	7849
7692			7787	7865	7772	7843	7794	7741
			7799	7866	7773	7777	7795	7852
			7800	7768	7778	7837	7796	7853
			7806	7833	7784		7805	7854
			7822		7788		7808	7855
			7823		7789		7809	7856
			7824		7797		7813	7858
			7825		7798		7814	7859
					7804		7816	7860
							7845	

(b) Data and simulation digit coincidences at TOF stations collected for the analysis.

State	Data		Simulation	
	TOF1	TOF2	TOF1	TOF2
Zero Abs. 172 MeV/c, Muon	624577	94722	771720	127245
Zero Abs. 200 MeV/c, Muon	384909	56314	370079	51822
Zero Abs. 240 MeV/c, Muon	314739	62546	1204155	261244
LiH 172 MeV/c, Muon	1282488	174405	718185	108777
LiH 200 MeV/c, Muon	1223560	177460	364587	45638
LiH 240 MeV/c, Muon	1239827	232982	1266073	236582

Aluminium vacuum windows separate the helium volume from the vacuum containing the absorber. The absorber itself is either a Lithium Hydride disk or an aluminium cask meant to contain liquid hydrogen, which has been pressed into service to contain various gases including helium, xenon, and neon. The scattering in all of the materials is summarized in Table 1.

The MICE LiH absorber is a disk, 65 mm in length (along the Z axis) with a 45 cm diameter with a composition of 81% ^{6}Li, 4% ^{7}Li, 14% ^{1}H with some trace amounts of Carbon, Oxygen and Calcium. The radiation length was calculated to be 70.34 g/cm^2 using the expression provided by the PDG [6] and the density has been measured to be 4.511$\pm$0.003 g/cm^2 based on measurements of a test mass with uncertainties of 1 g and the dimensions of 0.254 mm.

The scattering distribution widths predicted by Eq.10 for the absorber materials and the other materials in the channel are shown in Table 1. This shows that the vast majority of the scattering in the MICE channel takes place in the absorber for the LiH.

The MICE coordinate system maps the standard right handed co-ordinate system on to the MICE hall where $+y$ points towards the ceiling of the MICE hall, $+z$ points downstream which is also westward and $+x$ toward the south wall of the hall.

2 Data Collection

Six data sets were compiled during the ISIS user cycle 2015/04 at three different momenta; 172 MeV/c, 200 MeV/c, and 240 MeV/c; with and without the lithium hydride (LiH) absorber in place. These data sets were collected in parallel so that no more than two runs were collected at the same momentum to balance any systematic behaviours that may have appeared in ISIS running over the three nominal momenta. The runs collected during these time periods are listed in Table 2a. Table 2b shows the number of events that produce space points in TOF1 and TOF2 for the collected runs. Fig. 1 shows the MICE channel configuration.

3 Particle Selection

Data reconstruction and simulation was completed using MAUS (3.1.2). A comparison between the selected muons upstream is shown in Fig. 15. The bulk of the analysis relies on the data collected with the absorber to provide the scattering measurement and data without the absorber to provide an independent measurement of the detector reconstruction and beam behaviour. The simulation is then used for the prediction of scattering in the absorber material.

Prior to any higher order analysis a set of particles that are most likely to provide an unbiased scattering distribution must be selected from the data sample. The set of cuts used for the analysis is provided in Table 3 with the proportion of events selected from the absorber data sets. Only events that produce a space point in TOF1 and a trajectory in the upstream tracker are considered. Fig. 4 shows the effect of the selection where the number of events is the number of muons after the cut has been applied and sucessive cuts are added going from Fig. 4a to Fig. 4c.

3.1 Downstream Track Detection

A measurement of scattering requires a trajectory reconstructed in the downstream tracker. An event cannot be rejected outright however if the downstream trajectory is absent for two reasons; normalization of the scattering distribution and to allow the possibility of correcting of the acceptance. In the absence of a reconstructed track

Table 3: Simple particle selection criteria for data with survival rates for data in LiH, the cuts are applied sequentially with the population after sucessive cuts shown on each line.

		μ Beams, LiH abs.		
Selection	Description	172	200	240
Upstream track selection	There is one US track and at most one track in the DS tracker (If there is no DS track $\theta_X = \theta_Y = 45°$).	100.0 %	100.0 %	100.0 %
Diffuser cut	US tracks are projected to the diffuser position any track within the radius of the diffuser annuli is rejected	82.07 %	82.07 %	82.07 %
Fiducial selection	For projected US tracks $\sqrt{x^2+y^2} < r_0$ at plane 5 of DS tracker, where $x = x_0 + (\frac{dx}{dz}\Delta z)$, $y = y_0 + (\frac{dy}{dz}\Delta z)$ and $r_0 = 90$ mm.	3.69 %	3.69 %	3.69 %
χ^2 cut	χ^2/NDF of track is less than 4 up- & downstream	3.69 %	3.69 %	3.69 %
TOF timing selection	Select muons from run at the target momentum.	0.21 %	0.25 %	0.15 %

downstream of the absorber, an angle of $\pi/4$, well outside of the channel acceptance, is assigned to the event so that the scattering angle appears in an overflow bin.

3.2 TOF Selection and Momentum

If the particle has a time of flight between stations 0 and 1 ($\Delta\, t_{01}$) that falls outside of a window the particle is rejected. Time of flight distributions for the three beam settings are shown in Fig. 10a. The particles selected are shown in Fig. 4a. The time of flight is used to select muons from the beam with a given momentum at the absorber.

The momentum in the channel is calculated with

$$p = \frac{m}{\sqrt{\frac{t_\mu^2}{t_e^2} - 1}} \tag{14}$$

where t_μ and t_e are the time of flight of the muon and electron respectively. If the muon reaches the end of the channel the measurement is made using TOF1 and TOF2. In the case that no hit is recorded in TOF2 then the measurement is made using the upstream information from TOF0 and TOF1. Only the case of a TOF0/TOF1 measurement is a correction applied to account for the energy loss in the channel. The energy lost by muons in the channel is calculated using the Bethe-Bloch expression for the most probable energy loss [7]

$$\Delta_p = \xi\left[\ln\frac{2mc^2\beta^2\gamma^2}{I} + \ln\frac{\xi}{I} + j - \beta^2 - \delta(\beta\gamma)\right] \tag{15}$$

where

$$\begin{aligned} \xi &= (K/2)\langle Z/A\rangle z^2(x/B^2) \\ I &= \text{mean excitation energy} \\ j &= 0.2 \end{aligned} \tag{16}$$

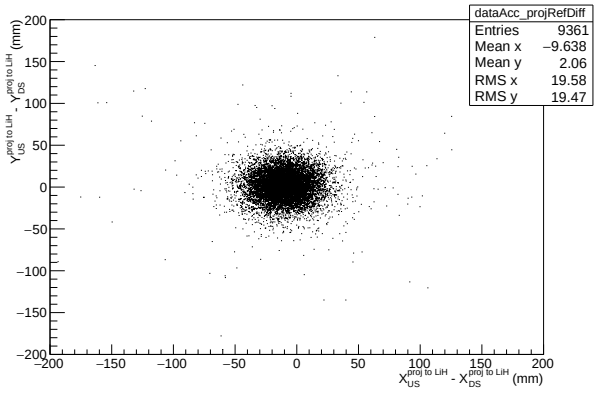

(a) X and Y distance between projected tracks at centre of absorber

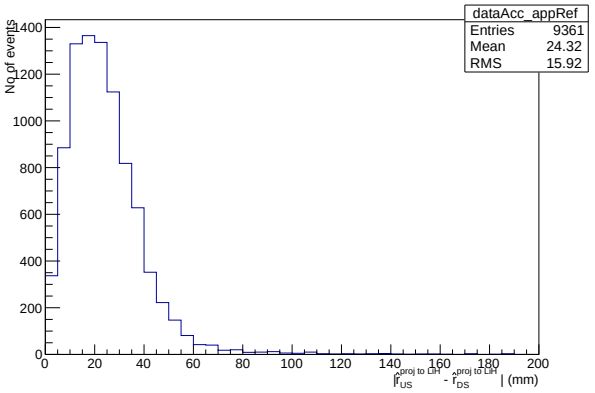

(b) Total distance between projected tracks at centre of absorber

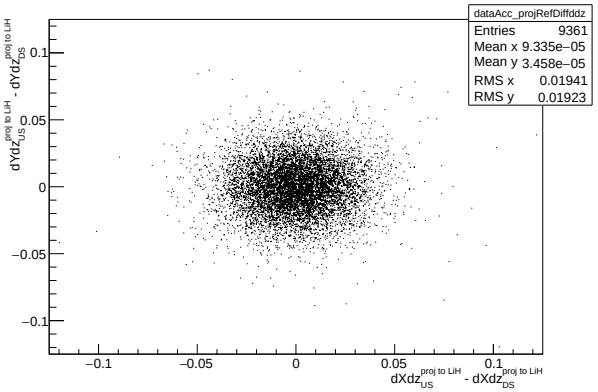

(c) $dXdz$ and $dYdz$ distance between projected tracks at centre of absorber

Figure 2: Total distance between projected tracks at centre of absorber with absorber in channel

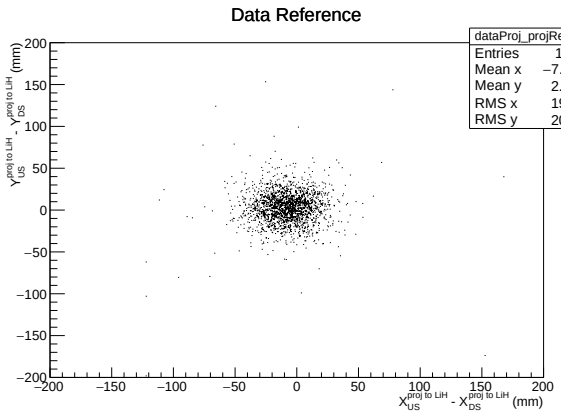

(a) X and Y distance between projected tracks at centre of absorber

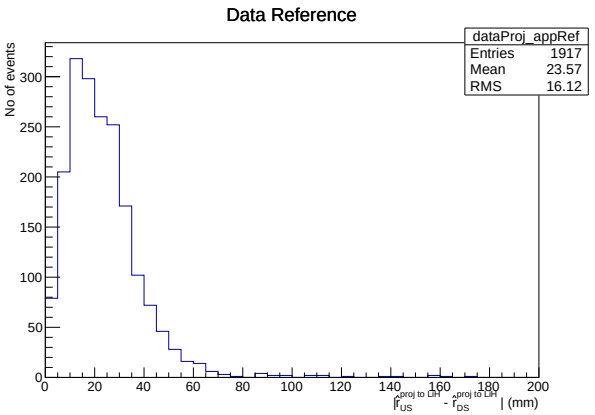

(b) Total distance between projected tracks at centre of absorber

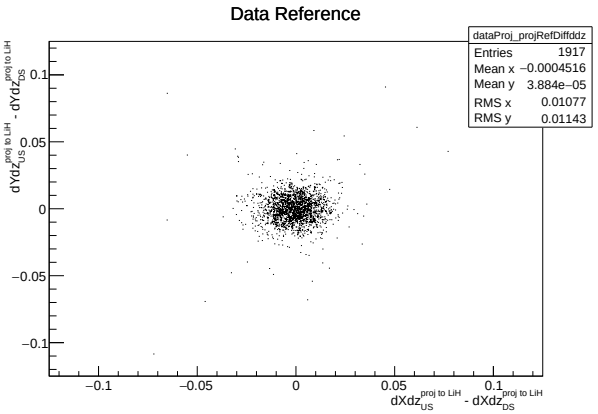

(c) $dXdz$ and $dYdz$ distance between projected tracks at centre of absorber

Figure 3: Total distance between projected tracks at centre of absorber with no absorber in channel

on a muon-by-muon basis and the agreement between the calculated momentum and that for Monte Carlo truth muons at the centre of the absorber is shown in Fig. 10c. An empircal fit between the corrected momentum and time of flight shown of the form

$$t_\mu = \frac{m}{p} + c \tag{17}$$

is made in figure 10b which will be used in section 7.

3.3 Fiducial Selection of Events

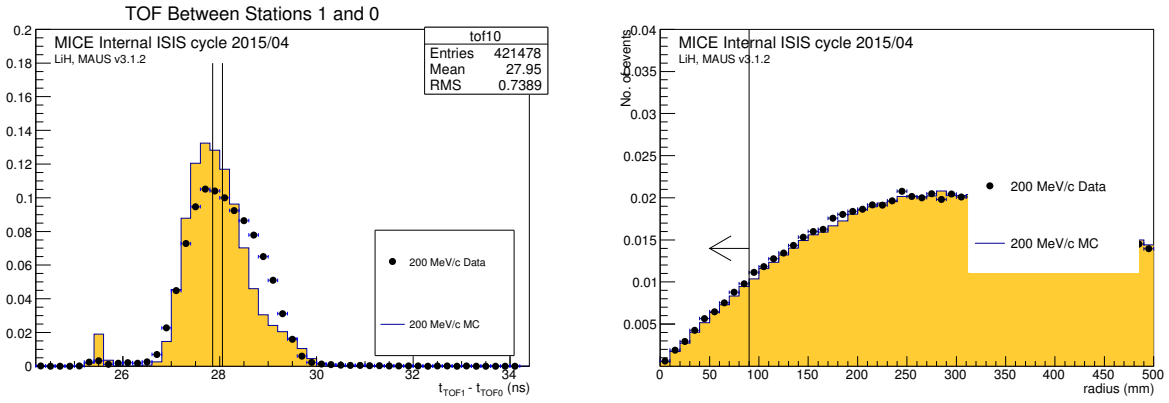

(a) Time of flight measured between first and second TOF stations for data and MC, muons between the two black lines are selected for the 200 MeV/c momentum data set.

(b) Projected position of muons at downstream station 5 for data and MC, muons to the left of the black line are selected.

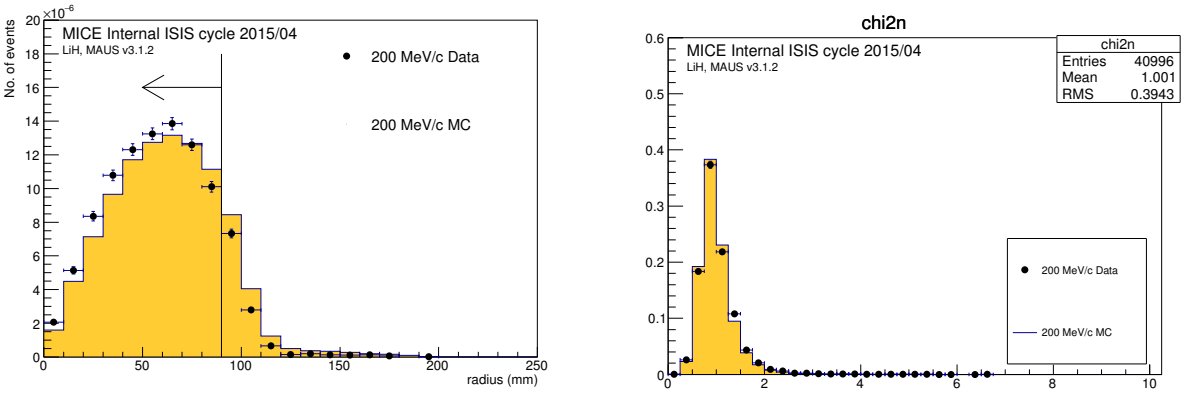

(c) Projected position of muons at the upstream face of the diffuser position for data and MC, muons to the left of the black line are selected.

(d) χ^2/NDF of tracks for data and MC, tracks with a values greater than 4 are rejected.

Figure 4: Effect of various selection cuts.

Finally, if the upstream track is projected to the downstream tracker station 5 and that track falls outside of the active radius of the detector,

$$\sqrt{x^2 + y^2} > r_0 \tag{18}$$

that particle is rejected. Here

$$x = x_0 + (\frac{dx}{dz} \times \Delta z) \quad (19)$$
$$y = y_0 + (\frac{dy}{dz} \times \Delta z) \quad (20)$$

and $r_0 = 90$ mm is assumed. To select upstream tracks that are suspected to produce downstream tracks contained within the tracker volume, all tracks are projected from the upstream tracker to the downstream tracker If the radial position of the projected track at the downstream tracker is greater than 90 mm then the track is rejected.

Upstream tracks are also propagated through the diffuser which is located immediately upstream of the upstream tracker. The diffuser, which is used to set the beam emittace, was fully retracted for all of the runs used to measure multiple scattering. However even in this position it is still possible for tracks to be transported through the diffuser ring in the retracted position and contained within the upstream tracker. This subset of tracks will have seen more material than the other selected tracks and therefore have lost more energy therefore if a track passes through the diffuser ring it is rejected. The particles selected are shown in Fig. 4c.

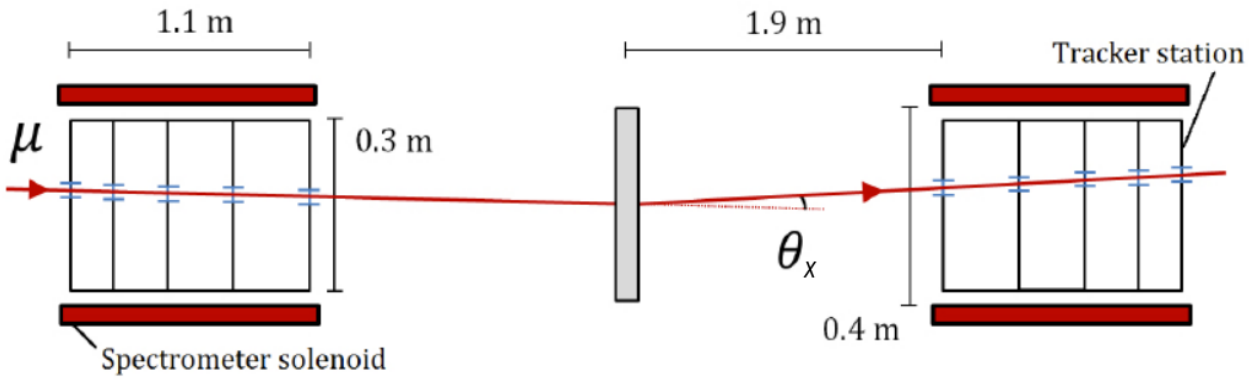

Figure 5: Illustrates the fiducial volume cut. Shows the upstream track projected to station 5 of the downsteam tracker. If the position of the track at end of the downstream tracker falls outside the active area of the tracker the track is rejected. Figure taken from

When analysing the data it was discovered that the two MICE trackers were misaligned. This can be seen clearly in Fig. 18a. If the trackers were aligned in the raw data then when tracks up- and downstream were extrapoled to the centre of the MICE channel the mean position in x and y would be zero. In the raw data there is an offset in the mean in x. The consequence of this is that the raw scattering distributions are skewed around 0.

Scattering is isotropic and no one direction should be favoured therefore the scattering distributions should be symmetric. To test this the asymmetry of the scattering distribution was calculated as

$$\text{Asymmetry} = \frac{i\text{th bin from left} - i\text{th bin from right}}{i\text{th bin from left} + i\text{th bin from right}}. \quad (21)$$

All upstream tracks were then rotated by a fixed angle and a scan in this angle was performed as shown in Fig. 8. The correction angles for the LiH data were -2.35 mrad (θ_Y) and 1.8 mrad (θ_X). For the empty channel data the angles were -0.75 mrad (θ_Y) and -1.25 mrad (θ_X). Based on this scan the correction angle was then applied to all of the collected data. All subsequence plots will include this correction which removes the effect of the tracker misalignment.

The effect of the selection criteria on the position and angle distributions in the 3-200 MeV/c data appear in

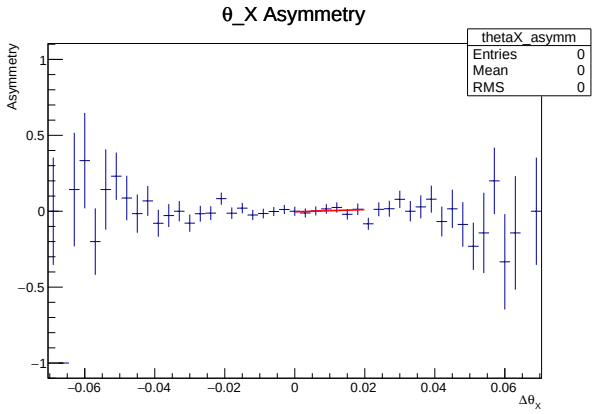

(a) Asymmetry in θ_X scattering distribution in LiH data

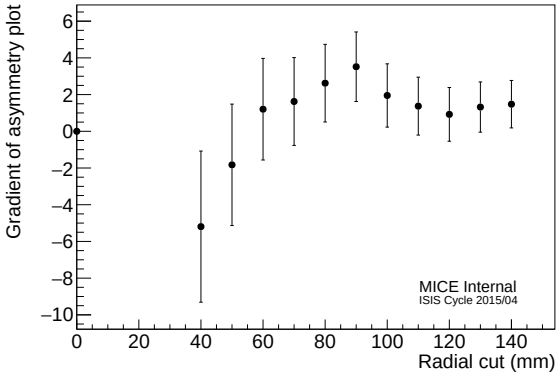

(b) Asymmetry in θ_X scattering distribution as a function of fiducial volume cut

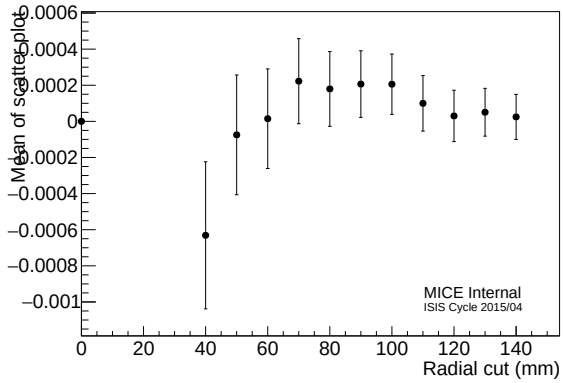

(c) Position of mean of θ_X scattering distribution as a function of fiducial volume cut

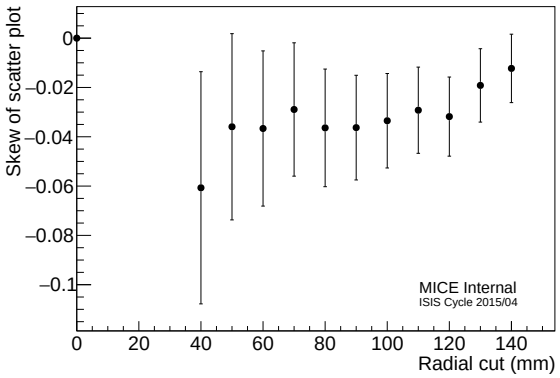

(d) Skewness of θ_X scattering distribution as a function of fiducal volume cut

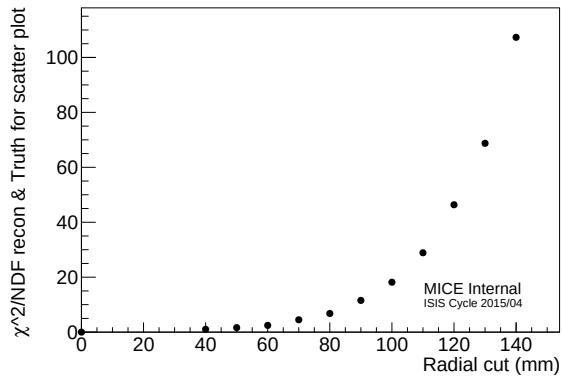

(e) χ^2/NDF of θ_X scattering distribution MC Truth and reconstruted as a function of fiducal volume cut

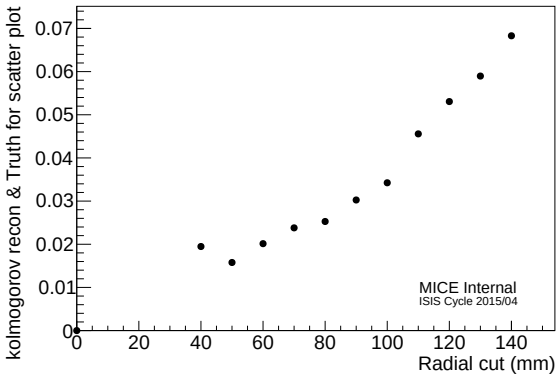

(f) Kolmogorov distance test between θ_X scattering distribution MC Truth and reconstruted as a function of fiducal volume cut

Figure 6: Test of the isotropic nature of scattering distributions with various quanities as a function of fiducial cut.

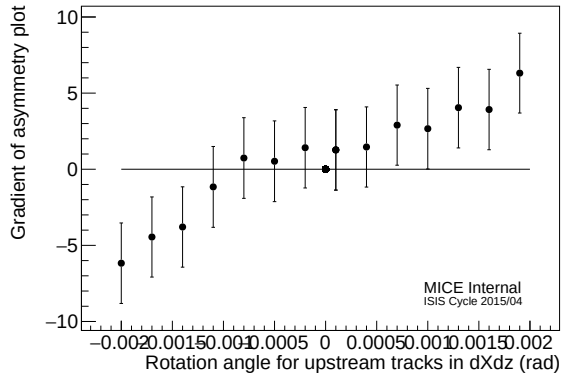

(a) Scan in asymmetry correction angle for θ_X in LiH data

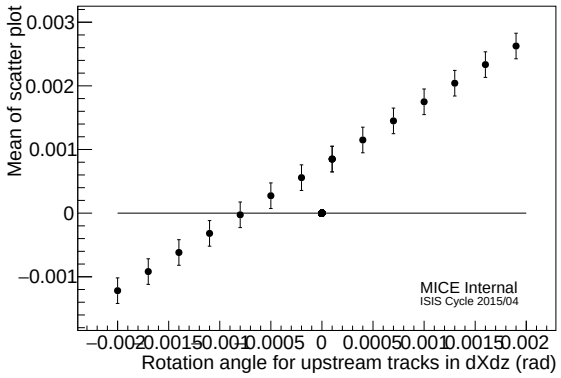

(b) Scan in mean correction angle for θ_X in LiH data

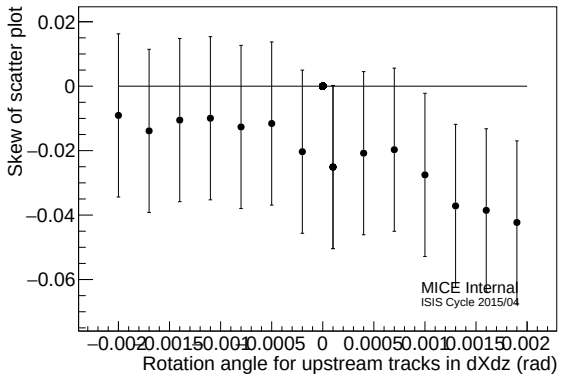

(c) Scan in skew correction angle for θ_X for LiH data

Figure 7: The angle applied to tracks is varied and the angle where the data crosses the x-axis can be clearly seen. At this point the scattering distribution is symmetric as expected. Plots are for 200 MeV/c muons.

Table 4: Time of flight selections between stations 1 and 2 made to correspond to specific axial momenta at the centre of the absorber.

(a) TOF for Muon Beams

Momentum (MeV/c)	lower limit (ns)	upper limit (ns)	Calculated $\langle p \rangle$ (MeV/c)	Standard deviation (MeV/c)
172	28.55	28.75	171.90±0.08	6.11±0.05
200	27.86	28.06	200.11±0.09	7.91±0.06
240	27.15	27.25	239.35±0.17	11.86±0.12

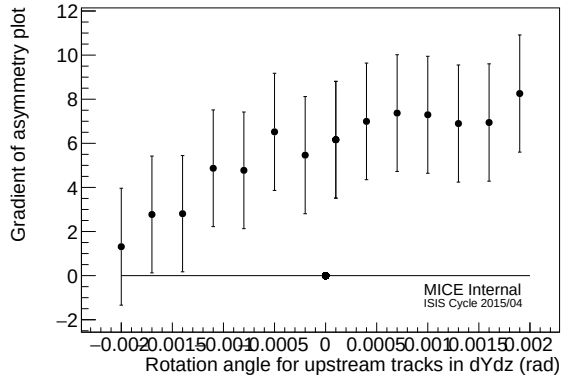

(a) Scan in asymmetry correction angle for θ_Y in LiH data

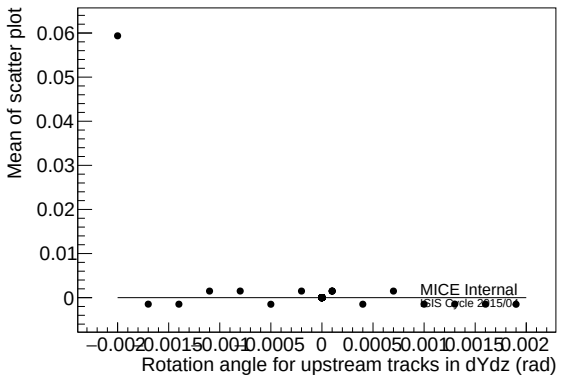

(b) Scan in mean correction angle for θ_Y in LiH data

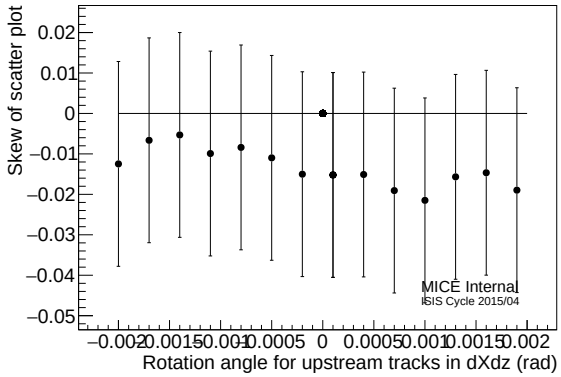

(c) Scan in skew correction angle for θ_Y for LiH data

Figure 8: The angle applied to tracks is varied and the angle where the data crosses the x-axis can be clearly seen. At this point the scattering distribution is symmetric as expected. Plots are for 200 MeV/c muons.

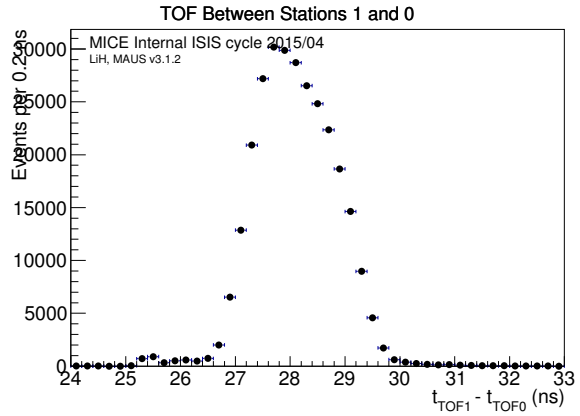

(a) TOF distributions of muon beams.

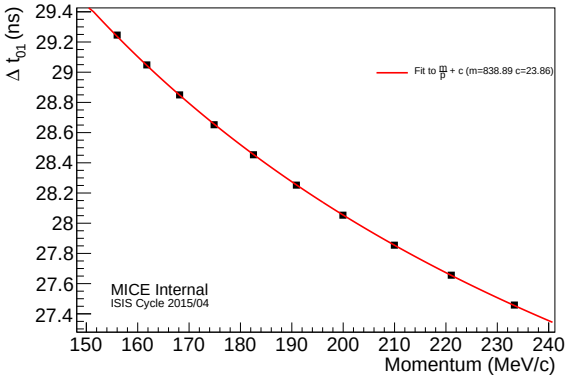

(b) Mean momentum by TOF

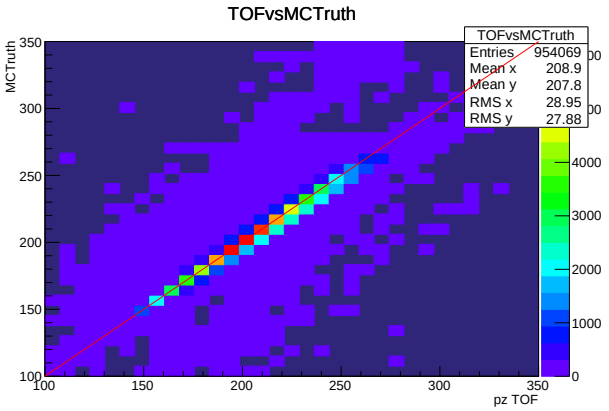

(c) Momentum from TOF calculation.

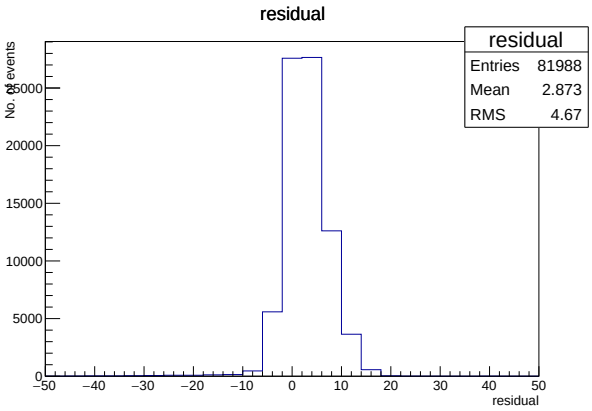

(d) Momentum residuals

Figure 9: The time of flight and momentum distributions for the muon beam with a comparison to the MC Truth P

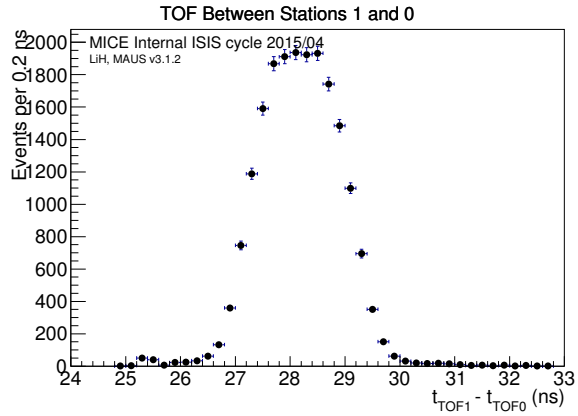

(a) TOF distributions of muon beams.

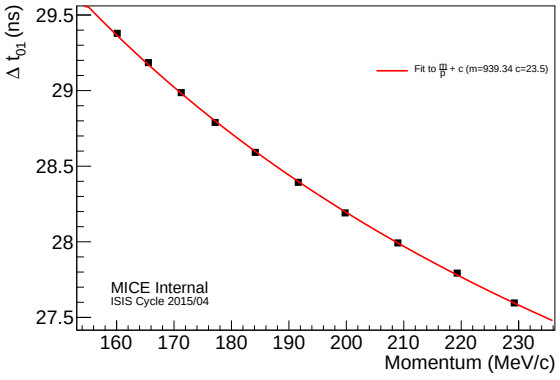

(b) Mean momentum by TOF

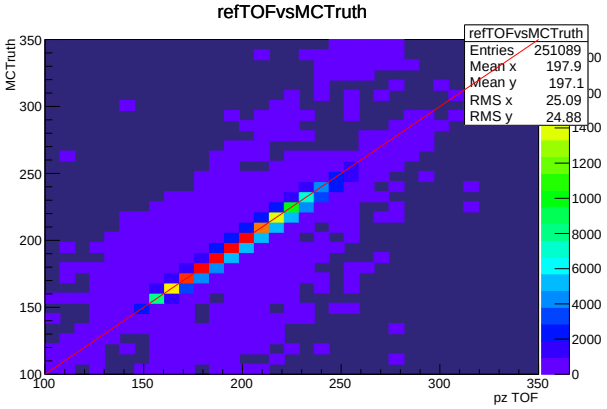

(c) Momentum from TOF calculation.

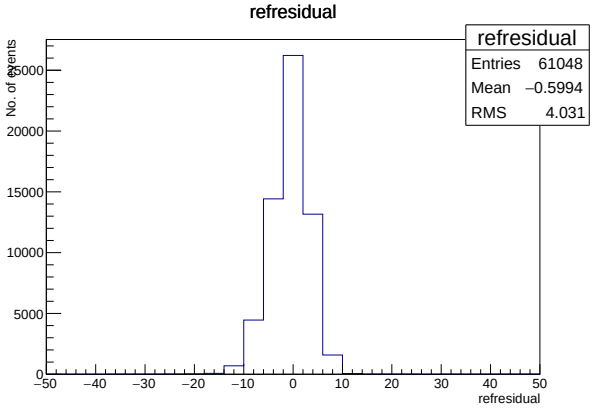

(d) Momentum residuals

Figure 10: The time of flight and momentum distributions for the muon beam with a comparison to the MC Truth P for the empty channel data and MC.

Fig.12 and Fig.14 respectively. The scattering distributions for the LiH data appears in Fig.17a, for and for data taken with no absorber in Fig.17b.

3.4 Selection Acceptance

A reconstruction acceptance can be estimated from the simulation by taking the ratio between the number of events for a true angle between θ_i and $\theta_i + \Delta\theta$.

$$\text{acceptance} = \frac{\text{No. of tracks in } \theta \text{ bin from MC Truth that are reconstructed}}{\text{No. of tracks in } \theta \text{ bin from MC Truth within angular acceptance}} \tag{22}$$

The reconstruction acceptance as a function of the projected scattering angles θ_X and θ_Y are shown in Fig.18. The acceptance depends strongly on the scattering angle and must be corrected on a bin by bin basis in the scattering distributions so the scattering angle distributions compiled from the data after all selections must be corrected by the acceptance measured from simulation after the same selection.

4 Analysis

4.1 Convolution with Alternative Models

The simplest approach for comparing data to simulation is to convolve the data from the zero absorber runs with the scattering distributions from various models and compare the result with the data including the absorber. The convolution is achieved by adding an angle sampled from the predicted scattering distribution in the absorber, shown in Fig. 19, to the angles determined from a given trajectory selected from the zero absorber data. The trajectory described with the sum of angles is extrapolated to the downstream tracker and those trajectories that do not appear in the downstream tracker are then treated as overflow events. The three models produce compatible predictions.

Because the zero absorber data sets are much smaller than the LiH data sets, the convolution was completed by sampling 10 different random angles from the source distribution for every data track selected from the empty absorber data. The resulting events are not statistically correlated so this procedure should have no impact on the treatment of statistical errors. This approach had the additional advantage that the resultant distribution is dominated by the model distribution of scattering in the absorber and the empty channel data is only used to related the model to measured tracks in the tracker.

The systematic uncertainties are calculated and summed on a bin by bin level. Plots of the reconstructed data with the empty absorber data and simulation of scattering in the absorber are shown in Fig. 20 at 200 MeV/c.

4.2 Deconvolution

The true scattering distributions must be unfolded from the measured raw scattering distributions. This is to remove the effects introduced by scattering due to other elements in the MICE detector, taking into account the tracker resolution. The unfolding step employs Gold's deconvolution algorithm, to extract the true scattering due to the absorber material as was described in [8]. This technique is employed in nuclear γ-ray spectroscopy and image restoration. This method had the advantage over other methods in that it did not rely on MC or scattering models and was a purely data driven technique making use of all of the data collected.

The method iterates over:

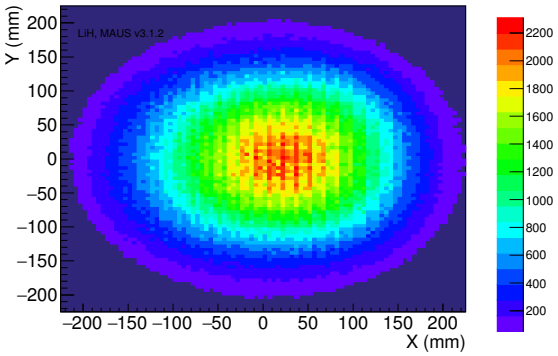

(a) LiH data with US tracks

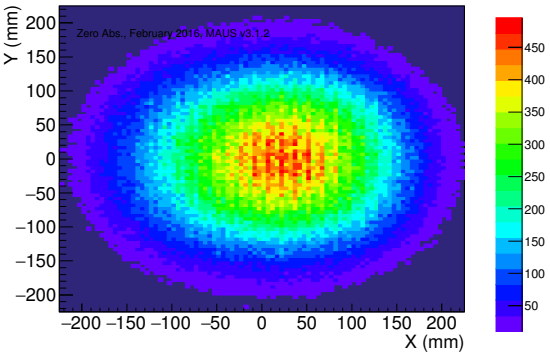

(b) Zero absorber data with US tracks

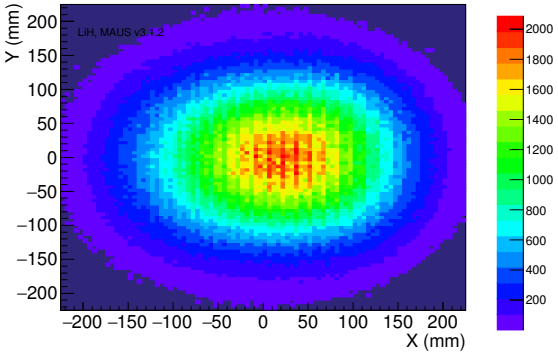

(c) LiH data passing TOF selection

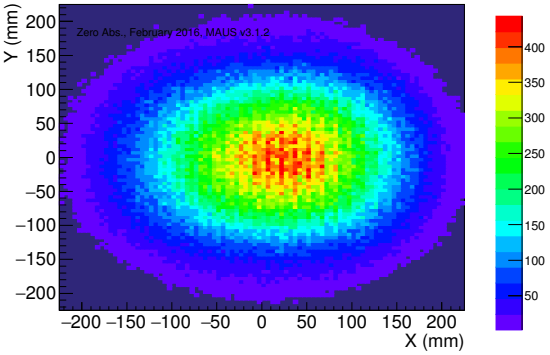

(d) Zero absorber data passing TOF selection

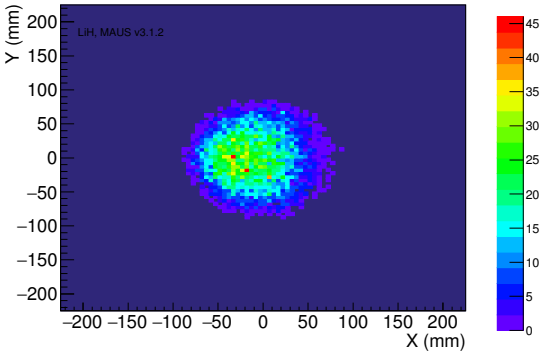

(e) LiH data passing all selections

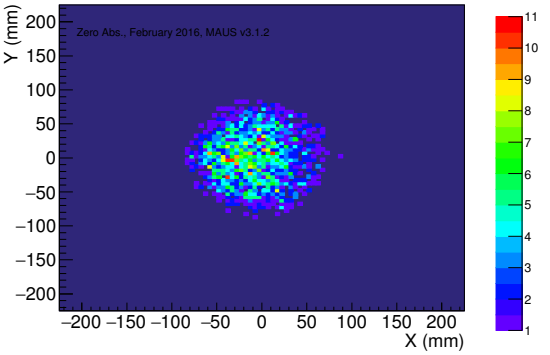

(f) Zero absorber data passing all selections.

Figure 11: Upstream position distributions for a 200 MeV/c muon beam in the LiH data and the zero absorber beam after particle selection at the upstream reference plane.

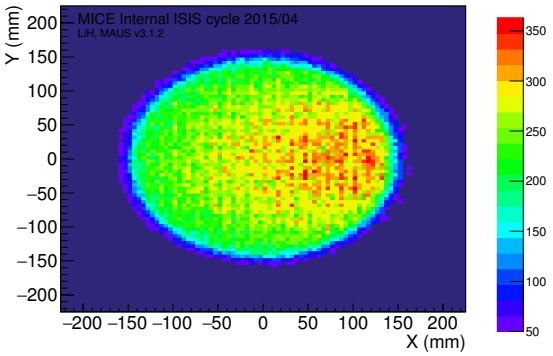

(a) LiH data with US tracks

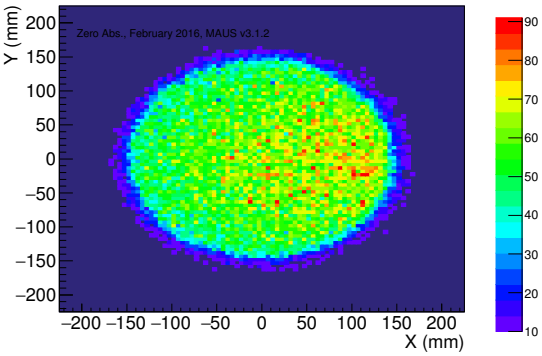

(b) Zero absorber data with US tracks

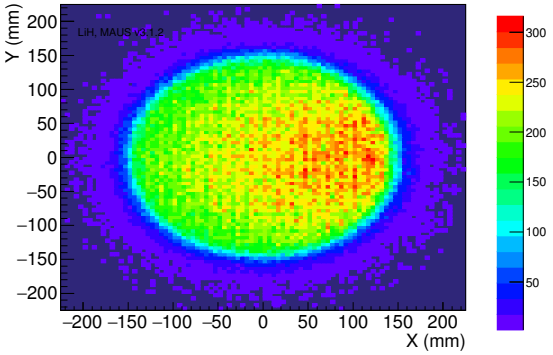

(c) LiH data passing TOF selection

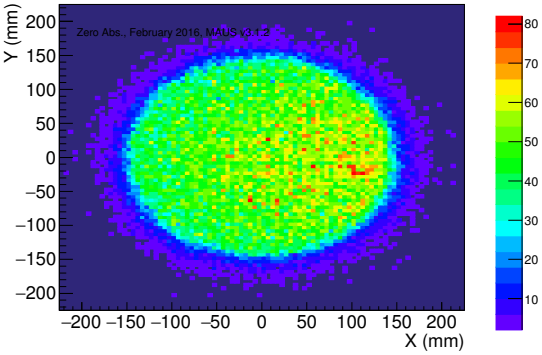

(d) Zero absorber data passing TOF selection

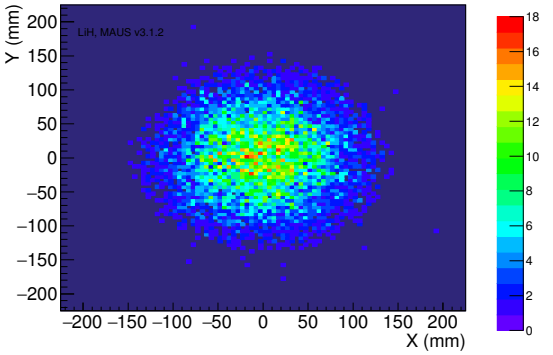

(e) LiH data passing all selections

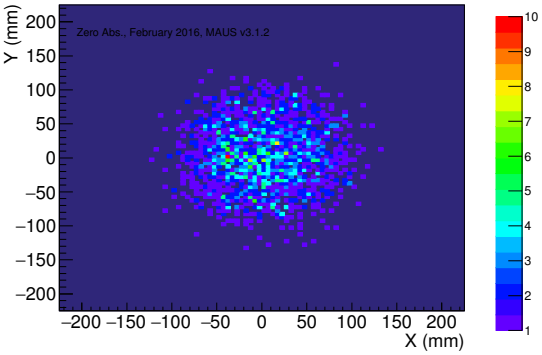

(f) Zero absorber data passing all selections.

Figure 12: Downstream position distributions for a 200 MeV/c muon beam in the LiH data and the zero absorber beam after particle selection at the downstream reference plane.

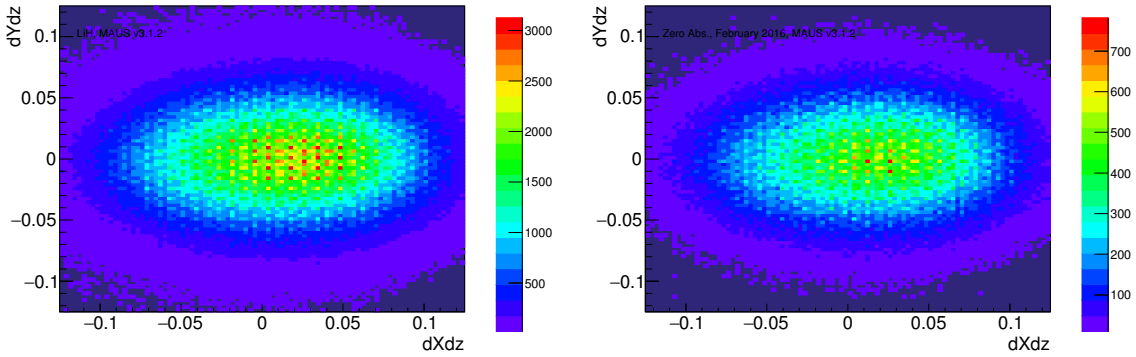

(a) LiH data with US tracks

(b) Zero absorber data with US tracks

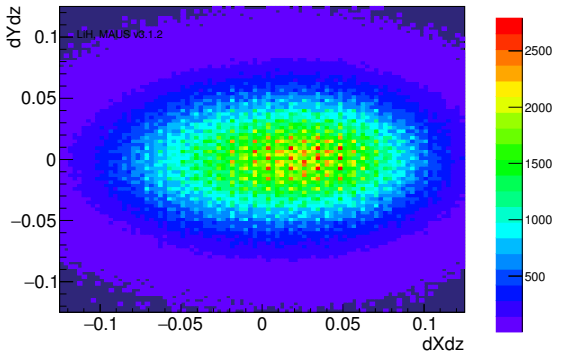

(c) LiH data passing TOF selection

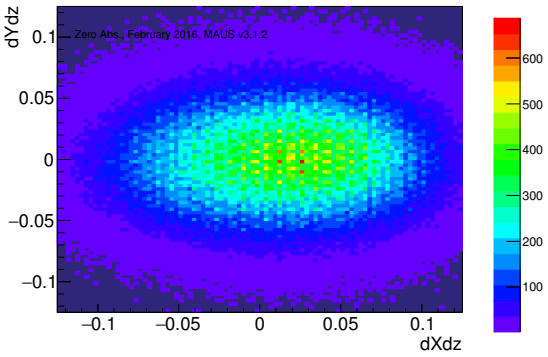

(d) Zero absorber data passing TOF selection

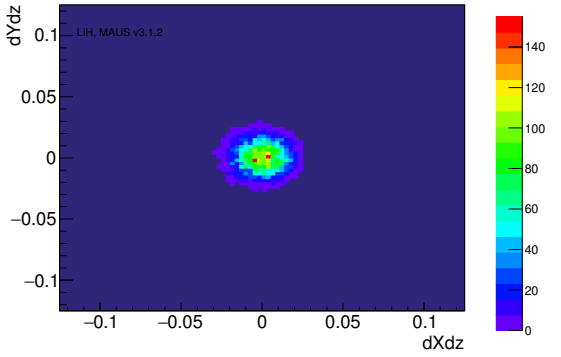

(e) LiH data passing all selections

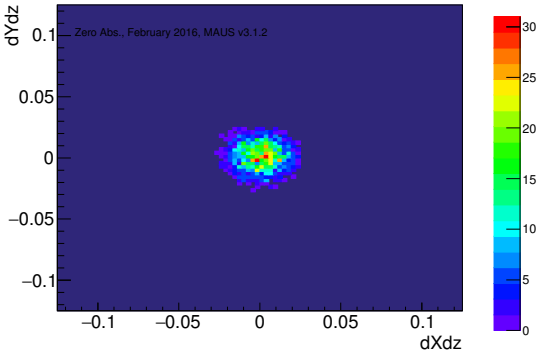

(f) Zero absorber data passing all selections.

Figure 13: Upstream angle distributions for a 200 MeV/c muon beam in LiH data and the zero absorber beam after particle selection at the upstream reference plane.

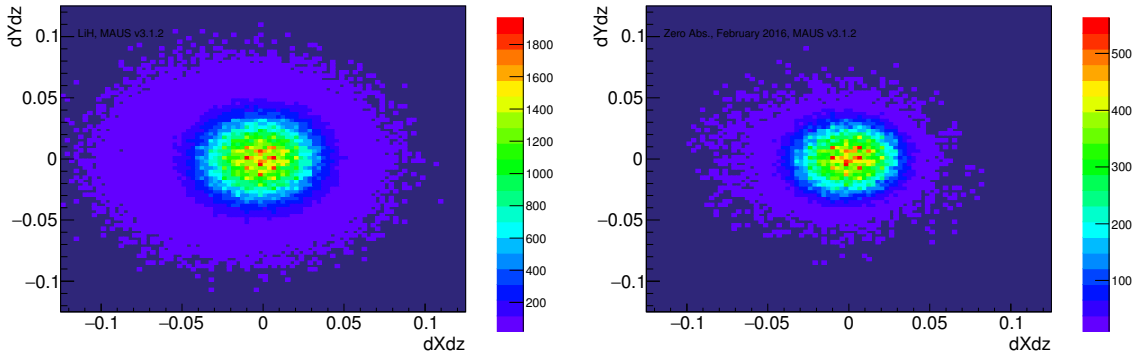

(a) LiH data with US tracks

(b) Zero absorber data with US tracks

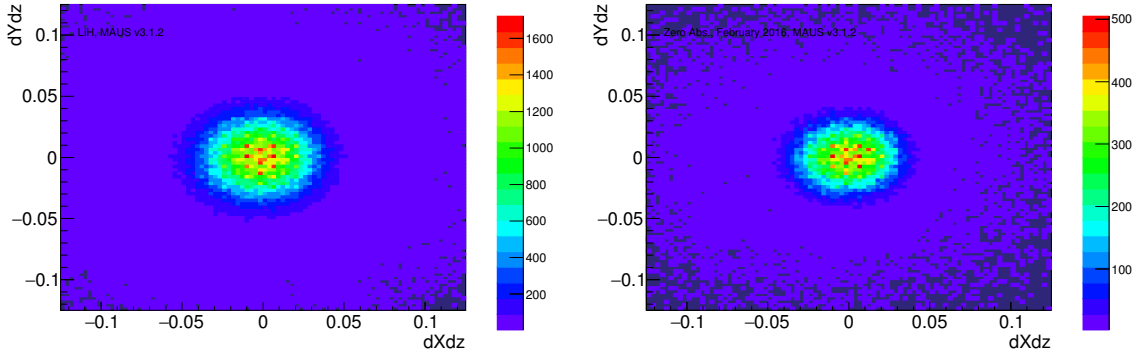

(c) LiH data passing TOF selection

(d) Zero absorber data passing TOF selection

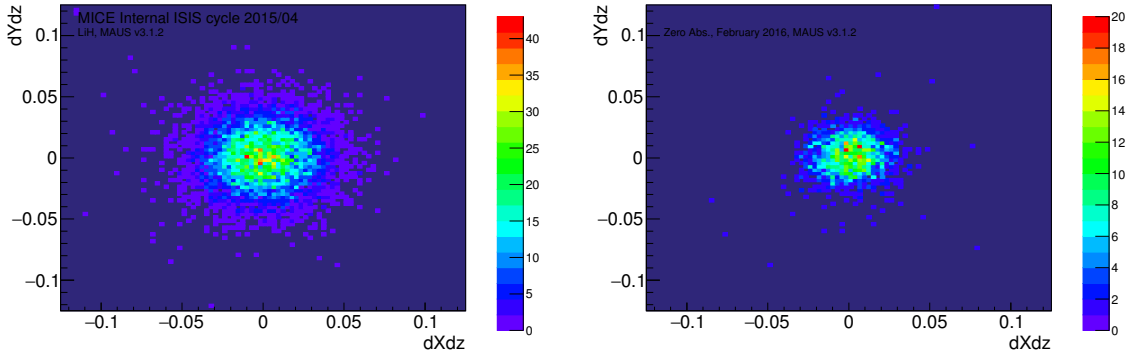

(e) LiH data passing all selections

(f) Zero absorber data passing all selections.

Figure 14: Downstream angle distributions for a 200 MeV/c muon beam in LiH data and the zero absorber beam after particle selection at the downstream reference plane.

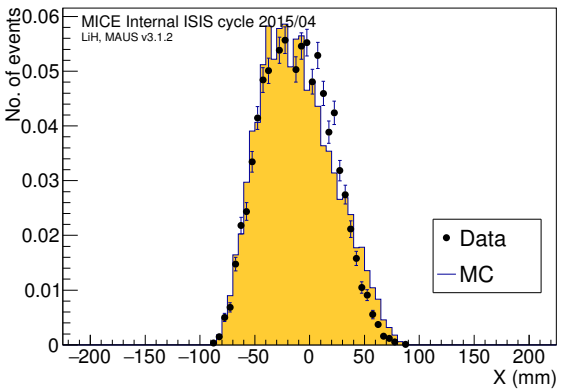

(a) Selected muons X distribution at upstream reference plane.

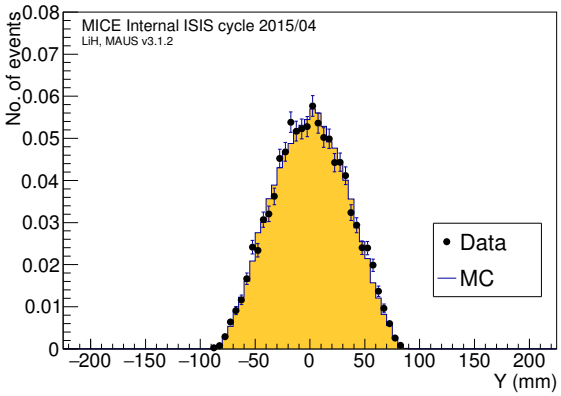

(b) Selected muons Y distribution at upstream reference plane.

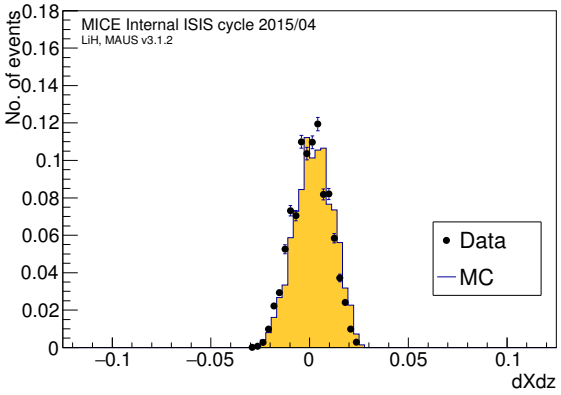

(c) Selected muons $dXdz$ distribution at upstream reference plane.

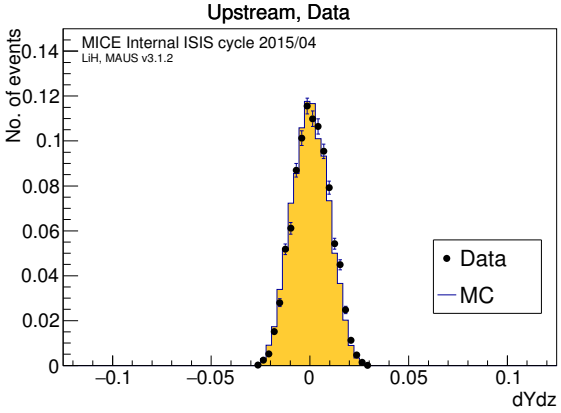

(d) Selected muons $dYdz$ distribution at upstream reference plane.

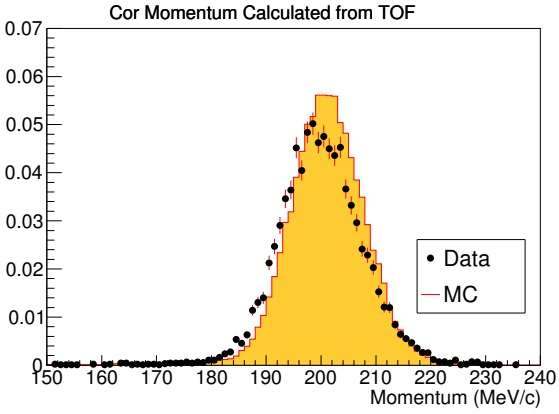

(e) Selected muons p_z distribution at the centre of the absorber

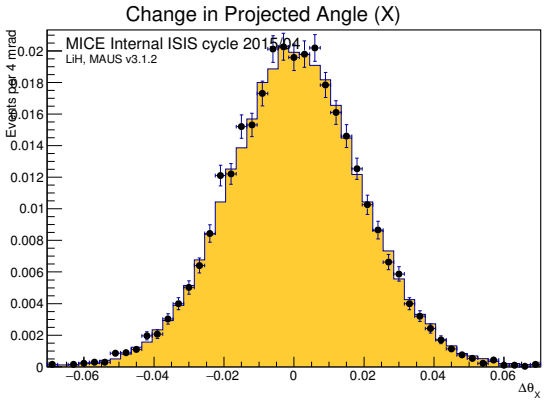

(f) Selected muons θ_X distribution

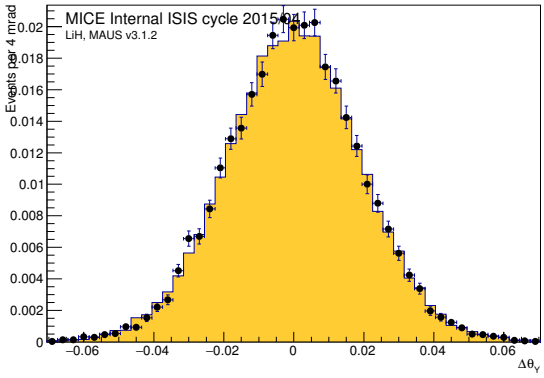

(g) Selected muons θ_Y distribution

Figure 15: Comparison between MC and data for selected muons at the upstream reference plane.

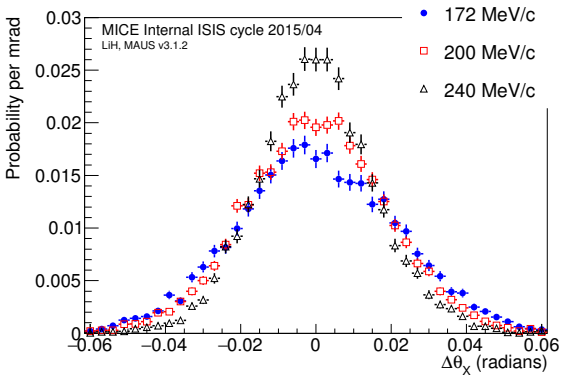

(a) Scattering of μ^+in LiH

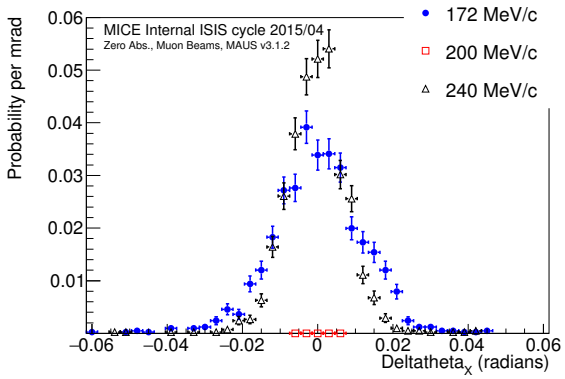

(b) Scattering of μ^+ in null absorber

Figure 16: Measured $\Delta\theta_X$ distributions in the LiH absorber (left) and Zero (right) absorber data sets at the three different momentum settings.

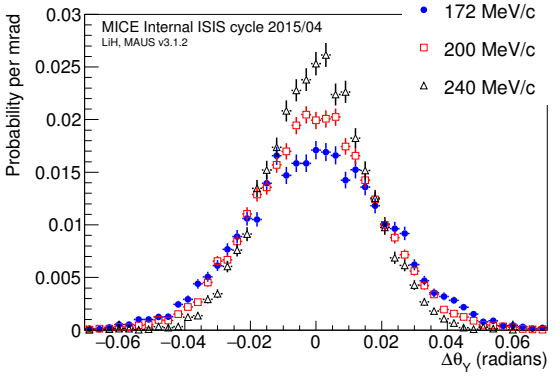

(a) Scattering of μ^+in LiH

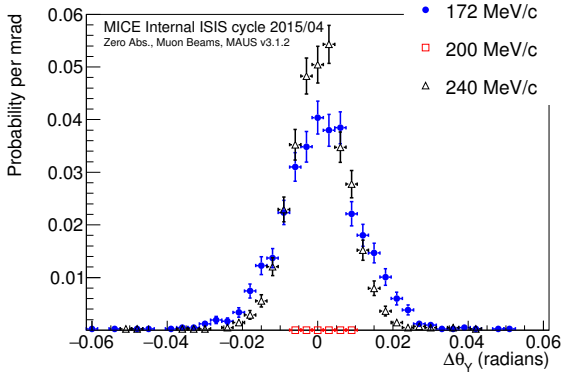

(b) Scattering of μ^+ in null absorber

Figure 17: Measured $\Delta\theta_Y$ distributions in the LiH absorber (left) and Zero (right) absorber data sets at the three different momentum settings.

(a) Efficiency in θ_X

(b) Efficiency in θ_Y

Figure 18: The fraction of events reconstructed by the trackers as a function scattering angle after event selection.

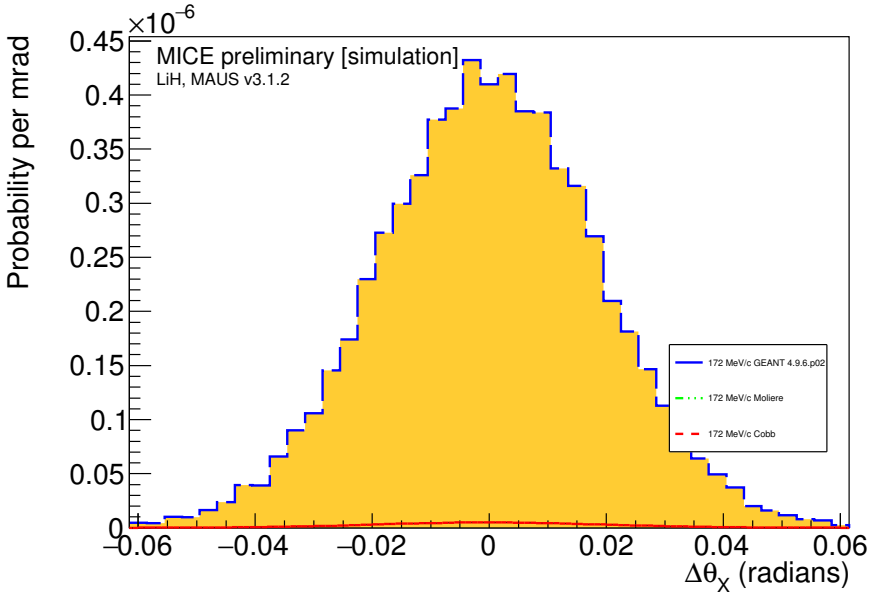

Figure 19: Theoretical scattering distributions calculated using different multiple scattering implementations.

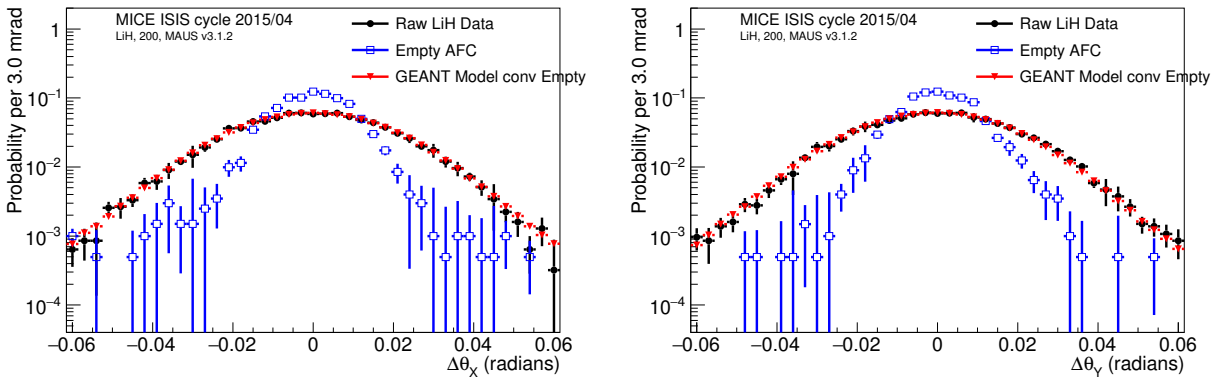

(a) Scattering about the x-axis

(b) Scattering about the y-axis

Figure 20: Scattering distributions reconstructed from the 200 MeV/c muon beam with the LiH absorber in place compared to two different scattering models in LiH convolved with the scattering data taken without the LiH absorber in place.

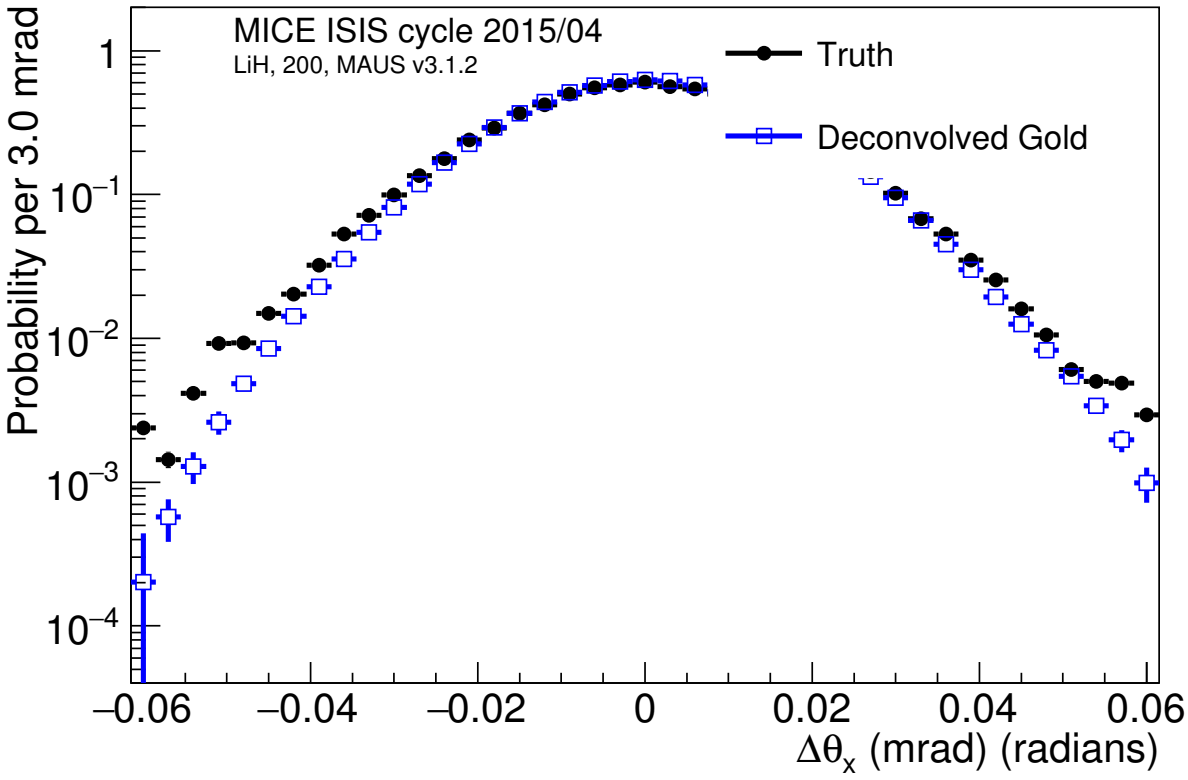

Figure 21: Scattering distributions from MC Truth and deconvolved reconstructed simulation.

$$x_i^{(k+1)} = \frac{x'_i}{\sum_{m=0}^{N-1} H'_{im} x_m^{(k)}} x_i(K) \tag{23}$$

where

$$\begin{aligned} i &= 0, 1, ..., N-1, \\ k &= 1, 2, 3, ..., L, \\ x^0 &= [1, 1..., 1]^T \end{aligned} \tag{24}$$

and where L is the number of iterations. A complete description of the method is given in appendix A.

As a cross check the scattering distribution from the MC Truth simulation was compared to the scattering distribution determined with the Gold deconvolution using reconstructed simulation data. The result is shown in Fig. 22 which illustrates the deconvolution proceedure recovering the input Truth scattering distribution.

5 Systematics

Before summarizing the results of the study, the systematic uncertainties will be discussed. Five different contributions to the systematic uncertainty are considered here; the effect of variations in the time of flight due to the resolution and momentum calibration, of variations in the measured alignment, variations in the fiducial radius, variations in the angle definition and the effect of pion contaimination in the muon beam. The

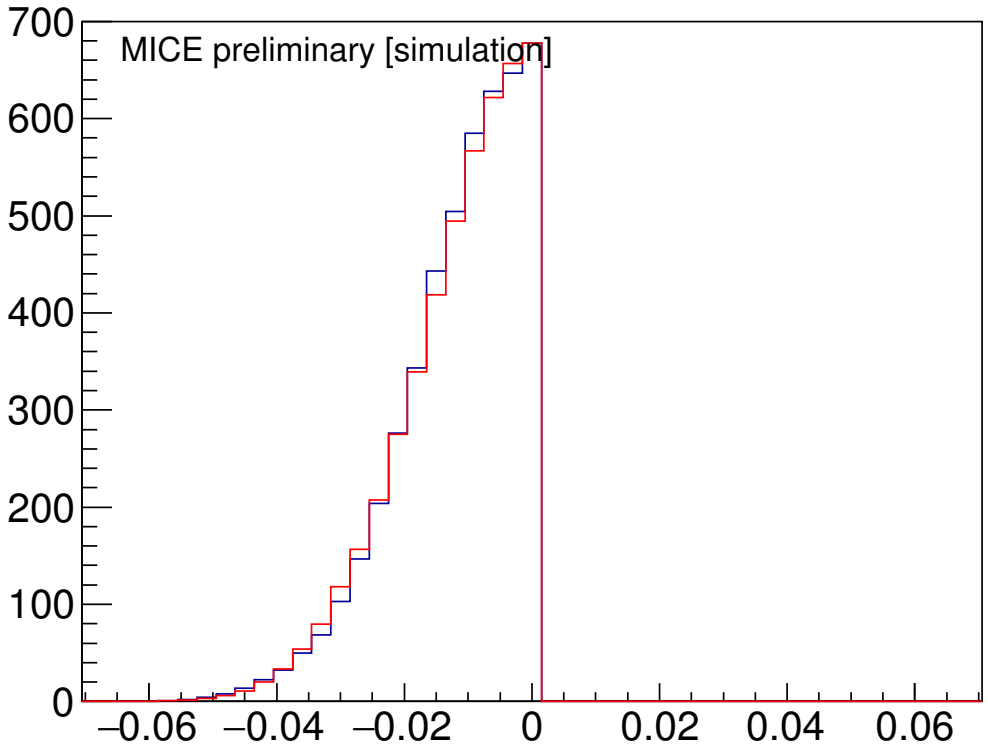

Figure 22: Scattering distributions from the deconvolved reconstructed simulation is folded around the central bin to compare the left and right handsides.

discussions below present the uncertainties in the measured widths with the associated sensitivities using a standardized formulation

$$\sigma_{sys} = \sigma_\alpha \frac{d\Theta}{d\alpha} \approx \frac{\sigma_\alpha}{\Delta\alpha}\Delta\Theta \tag{25}$$

where $\Delta\Theta$ is the change in the distribution width that results from altering a parameter with a known error σ_α in the analysis or simulation by a quantity $\Delta\alpha$. Each of the systematics is defined from the difference imposed by a variation in the named effect multiplied by a scaling factor that represents the uncertainty in the effect divided by the imposed change. The systematics are added on a bin by bin basis to the uncertainties used in the calculation of the χ^2 shown in Section 6 using the same scaling factor. The contribution to a single bin is given by

$$\sigma_{sys,i} = \frac{dn_i}{d\alpha}\sigma_\alpha \approx \frac{\sigma_\alpha}{\Delta\alpha}\Delta n_i \tag{26}$$

The systematics are reported for two different cases; the projection about the X axis and the projection about the Y axis.

5.1 Time of Flight and Momentum Sensitivity

A significant systematic uncertainty is due to the TOF selection criteria which directly impacts the momentum range of the particles used in the scattering measurement. The scale is set by the 70 ps resolution of the time of flight measurements. The effect of particles incorrectly appearing inside or outside of the 200 ps selection window is determined by offsetting the empty channel data by 200 ps and the difference in the measured scattering width, scaled by a factor of $\sigma_\alpha/\Delta\alpha = 129\ ps/200\ ps$, is treated as the systematic uncertainty. This is only relevant for the deconvolved data as in this case the width and shape of the empty channel scattering distribution is being used to determine the width and shape of the LiH scattering distribution. The uncertainties shown in Table 5b indicate that the uncertainties in the momentum are less than 4% of the measured scattering width and makes up the bulk of the systematic uncertainty.

Table 5: Sensitivity to variations in time of flight determined from offsets of ± 400 ns. Uncertainties are determined assuming a 70 ps TOF detector resolution and a 100 ps momentum calibration uncertainty.

(a) Uncertainties without deconvolution.

		$\Delta\theta_X$			$\Delta\theta_Y$			$\langle\theta^2_{Scatt}\rangle$		
Abs.	$\langle p\rangle$	$\Delta\Theta$ (mrad)	σ_{sys} (mrad)	σ_{sys}/Θ	$\Delta\Theta$ (mrad)	σ_{sys} (mrad)	σ_{sys}/Θ	$\Delta\Theta$ (mrad)	σ_{sys} (mrad)	σ_{sys}/Θ
LiH	171.9±0.08	-1.4	0.3	0.01	-1.6	0.3	0.02	-1.6	0.3	0.01
LiH	200.11±0.09	-1.7	0.4	0.02	-1.8	0.4	0.02	-1.9	0.4	0.02
LiH	239.4±0.2	-1.5	0.3	0.02	-1.7	0.4	0.02	-1.4	0.3	0.01

(b) Uncertainties after deconvolution.

		$\Delta\theta_X$			$\Delta\theta_Y$			$\langle\theta^2_{Scatt}\rangle$		
Abs.	$\langle p\rangle$	$\Delta\Theta$ (mrad)	σ_{sys} (mrad)	σ_{sys}/Θ	$\Delta\Theta$ (mrad)	σ_{sys} (mrad)	σ_{sys}/Θ	$\Delta\Theta$ (mrad)	σ_{sys} (mrad)	σ_{sys}/Θ
LiH	171.9±0.08	-1.2	0.3	0.01	-2.0	0.4	0.02	-1.6	0.3	0.01
LiH	200.11±0.09	-1.8	0.4	0.02	-1.7	0.4	0.02	-2.2	0.5	0.02
LiH	239.4±0.2	-1.6	0.3	0.03	-1.6	0.3	0.03	-1.4	0.3	0.01

5.2 Alignment

Uncertainties in the alignment have a direct effect on the angles measured by the tracker. The alignment of the MICE trackers is characterized by four parameters defining offsets, with an uncertainty of 0.2 mm, and angles, with an uncertainty of 0.07 mrad in the X-Z and Y-Z planes; the z position of the tracker and rotations about the z axis are not accessible to the alignment. The alignment of the upstream tracker is independent of the downstream detector inflating the total number of parameters to eight. To assess the effect on the MCS widths, a number of pseudo experiments have been run which vary the values of all of the alignment parameters within the errors. The uncertainties in the scattering width is extracted from the distributions of the measurements from the pseudo-experiments. After this is complete, the contributed uncertainty from the alignment is at the sub-percent level relative to the scattering width. The contribution has been included in the quoted systematic.

Table 6: Sensitivity to the alignment taken from the maximum variation of the alignment from the generated pseudo experiments

(a) Uncertainties without deconvolution.

		$\Delta\theta_X$			$\Delta\theta_Y$			$\langle\theta^2_{Scatt}\rangle$		
Abs.	$\langle p\rangle$	$\Delta\Theta$ (mrad)	σ_{sys} (mrad)	σ_{sys}/Θ	$\Delta\Theta$ (mrad)	σ_{sys} (mrad)	σ_{sys}/Θ	$\Delta\Theta$ (mrad)	σ_{sys} (mrad)	σ_{sys}/Θ
LiH	171.9±0.08	-0.01	0.001	6e-05	0.02	0.003	0.0001	-0.0008	9e-05	0.0
LiH	200.11±0.09	0.02	0.004	0.0002	0.0009	0.0002	1e-05	-0.005	0.001	5e-05
LiH	239.4±0.2	-0.03	0.006	0.0004	-0.04	0.007	0.0005	-0.01	0.002	0.0001

(b) Uncertainties after deconvolution.

		$\Delta\theta_X$			$\Delta\theta_Y$			$\langle\theta^2_{Scatt}\rangle$		
Abs.	$\langle p\rangle$	$\Delta\Theta$ (mrad)	σ_{sys} (mrad)	σ_{sys}/Θ	$\Delta\Theta$ (mrad)	σ_{sys} (mrad)	σ_{sys}/Θ	$\Delta\Theta$ (mrad)	σ_{sys} (mrad)	σ_{sys}/Θ
LiH	171.9±0.08	-0.03	0.003	0.0002	0.02	0.003	0.0001	-0.03	0.003	0.0001
LiH	200.11±0.09	-0.03	0.006	0.0004	-0.008	0.002	0.0001	0.02	0.006	0.0002
LiH	239.4±0.2	-0.02	0.004	0.0003	-0.03	0.006	0.0005	0.03	0.006	0.0003

5.3 Fiducial

The choice of the fiducial region may systematically affect the results. A scan over the possible values of the fiducial radius was completed and the difference between the scattering width of the grid points adjacent to the selection values of 90 mm was used to set the uncertainty with a scaling factor based on the uncertainties in position and angle which are 0.495 mm and 0.56 mrad respectively. The differences measured from changes in the fiducial gradient are then scaled by 0.56 mrad/10 mrad = 0.056, and the differences measured from changes in the fiducial radius are scaled by 0.495 mm/20 mm = 0.0248 to get the systematic uncertainties for the fiducial selection. The scattering width is insensitive to the radial fiducial selection with systematic uncertainties on the sub-percent level.

5.4 Angle defintions

The definitions of the scattering angles are given in section 1.1. Equation 3 gives the definition of the projected scattering angles where

$$\mathbf{v} = \mathbf{s} \times \mathbf{u} \tag{27}$$

Table 7: Sensitivities to changes in the fiducial radial selection assuming a fiducial gradient of 12 mrad.

(a) Uncertainties without deconvolution.

		$\Delta\theta_X$			$\Delta\theta_Y$			$\langle\theta^2_{Scatt}\rangle$		
Abs.	$\langle p \rangle$	$\Delta\Theta$ (mrad)	σ_{sys} (mrad)	σ_{sys}/Θ	$\Delta\Theta$ (mrad)	σ_{sys} (mrad)	σ_{sys}/Θ	$\Delta\Theta$ (mrad)	σ_{sys} (mrad)	σ_{sys}/Θ
LiH	171.9±0.08	0.4	0.01	0.0005	0.1	0.003	0.0002	0.2	0.006	0.0002
LiH	200.11±0.09	0.1	0.004	0.0002	0.3	0.007	0.0004	0.3	0.007	0.0003
LiH	239.4±0.2	0.1	0.003	0.0002	0.03	0.0007	5e-05	0.1	0.003	0.0001

(b) Uncertainties after deconvolution.

		$\Delta\theta_X$			$\Delta\theta_Y$			$\langle\theta^2_{Scatt}\rangle$		
Abs.	$\langle p \rangle$	$\Delta\Theta$ (mrad)	σ_{sys} (mrad)	σ_{sys}/Θ	$\Delta\Theta$ (mrad)	σ_{sys} (mrad)	σ_{sys}/Θ	$\Delta\Theta$ (mrad)	σ_{sys} (mrad)	σ_{sys}/Θ
LiH	171.9±0.08	0.5	0.01	0.0007	0.6	0.01	0.0007	0.4	0.009	0.0003
LiH	200.11±0.09	0.3	0.008	0.0005	0.5	0.01	0.0007	0.4	0.009	0.0004
LiH	239.4±0.2	0.1	0.003	0.0003	0.08	0.002	0.0001	0.3	0.008	0.0004

Table 8: Sensitivities to changes in angle definition.

(a) Uncertainties without deconvolution.

		$\Delta\theta_X$			$\Delta\theta_Y$			$\langle\theta^2_{Scatt}\rangle$		
Abs.	$\langle p \rangle$	$\Delta\Theta$ (mrad)	σ_{sys} (mrad)	σ_{sys}/Θ	$\Delta\Theta$ (mrad)	σ_{sys} (mrad)	σ_{sys}/Θ	$\Delta\Theta$ (mrad)	σ_{sys} (mrad)	σ_{sys}/Θ
LiH	171.9±0.08	0.1	0.1	0.006	-0.002	0.002	9e-05	0.0	0.0	0.0
LiH	200.11±0.09	0.2	0.2	0.01	-0.2	0.2	0.01	0.0	0.0	0.0
LiH	239.4±0.2	0.2	0.2	0.02	-0.3	0.3	0.02	0.0	0.0	0.0

(b) Uncertainties after deconvolution.

		$\Delta\theta_X$			$\Delta\theta_Y$			$\langle\theta^2_{Scatt}\rangle$		
Abs.	$\langle p \rangle$	$\Delta\Theta$ (mrad)	σ_{sys} (mrad)	σ_{sys}/Θ	$\Delta\Theta$ (mrad)	σ_{sys} (mrad)	σ_{sys}/Θ	$\Delta\Theta$ (mrad)	σ_{sys} (mrad)	σ_{sys}/Θ
LiH	171.9±0.08	-0.1	0.1	0.007	0.2	0.2	0.01	0.0	0.0	0.0
LiH	200.11±0.09	0.08	0.08	0.005	0.06	0.06	0.004	0.0	0.0	0.0
LiH	239.4±0.2	0.05	0.05	0.004	0.1	0.1	0.008	0.0	0.0	0.0

where $\mathbf{s}$ is arbitrary defined as $\mathbf{s} = (0, -1, 0)$. This expression defines the plane which contains the upstream track. While there are an infinite number of planes that contain this track the above definition is used in the analysis with the arbitrarily defined $\mathbf{s}$. When considering the error introduced with this definition $\mathbf{s}$ is rotated between 0 and 180° degrees around the x-axis with the analysis repeated at each point. Fig. 23 shows the measured scattering angle as a function of $\mathbf{s}$ for each rotated definition of $\mathbf{s}$. The resulting change in measured scattering angle is small and the maximum change is smaller than the total systematic error from the other sources discussed therefore MICE is insensitive to any change in this definition.

The analysis was repeated with an angle definitions of 20° and 140° and the systematic error was taken to be the difference between these two definitions with the results reported in table 8

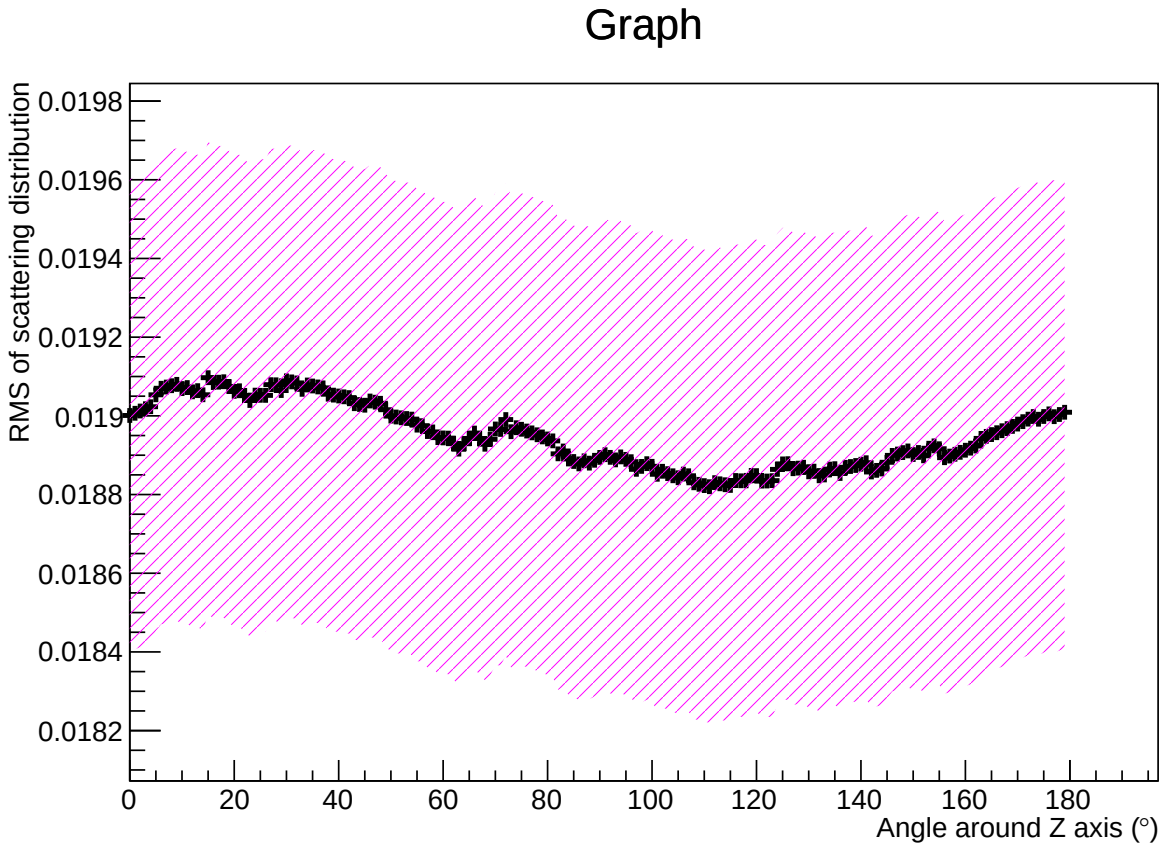

Figure 23: Change in measured width of θ_y scattering distribution for change in definition of plane vector $\mathbf{s}$. Band shows all other systematic errors.

5.5 Pion Contamination

The MICE muon beam has pion contamination with an upper limit of $f_\pi < 1.4\%$ at 90 % C.L. [9]. To measure the effect of this contamination on the scattering measurment for muons a Monte Carlo study was performed. The measurement was made with a simulation of the real MICE muon beam and a purely muon sample with the systematic error being the difference between the two results and are reported in table 9

Table 9: Sensitivities to pion contamination.

(a) Uncertainties without deconvolution.

		$\Delta\theta_X$			$\Delta\theta_Y$			$\langle\theta^2_{Scatt}\rangle$		
Abs.	$\langle p\rangle$	$\Delta\Theta$ (mrad)	σ_{sys} (mrad)	σ_{sys}/Θ	$\Delta\Theta$ (mrad)	σ_{sys} (mrad)	σ_{sys}/Θ	$\Delta\Theta$ (mrad)	σ_{sys} (mrad)	σ_{sys}/Θ
LiH	171.9±0.08	-0.0	0.0	0.0	-0.0	0.0	0.0	0.0	0.0	0.0
LiH	200.11±0.09	-0.0	0.0	0.0	-0.0	0.0	0.0	0.0	0.0	0.0
LiH	239.4±0.2	0.0	0.0	0.0	-0.0	0.0	0.0	0.0	0.0	0.0

(b) Uncertainties after deconvolution.

		$\Delta\theta_X$			$\Delta\theta_Y$			$\langle\theta^2_{Scatt}\rangle$		
Abs.	$\langle p\rangle$	$\Delta\Theta$ (mrad)	σ_{sys} (mrad)	σ_{sys}/Θ	$\Delta\Theta$ (mrad)	σ_{sys} (mrad)	σ_{sys}/Θ	$\Delta\Theta$ (mrad)	σ_{sys} (mrad)	σ_{sys}/Θ
LiH	171.9±0.08	0.0	0.0	0.0	0.0	0.0	0.0	0.0	0.0	0.0
LiH	200.11±0.09	-0.0	0.0	0.0	0.0	0.0	0.0	0.0	0.0	0.0
LiH	239.4±0.2	-0.0	0.0	0.0	-0.0	0.0	0.0	0.0	0.0	0.0

Table 10: Measurements of distribution widths and the χ^2 comparisons between data and two different implementations of multiple scattering. The χ^2 were calculated using number of bins as number of degrees of freedom. Statistical uncertainties alone have been given.

(a) Measurements in Lithium Hydride

p	Angle	Θ_{Data} (mrad)	Θ_{G4} (mrad)	χ^2	Θ_{CC} (mrad)	χ^2
171.9±0.08	θ_X	20.89±0.26±0.33	15.93±0.1	2359.5 / 35	16.14±0.11	1986.1 / 35
171.9±0.08	θ_Y	20.58±0.24±0.35	15.62±0.1	2755.7 / 35	16.25±0.11	1727.8 / 35
200.11±0.09	θ_X	18.2±0.17±0.42	14.25±0.07	3105.5 / 35	14.58±0.08	2046.8 / 35
200.11±0.09	θ_Y	17.99±0.17±0.42	14.26±0.08	3102.2 / 35	14.74±0.08	1979.5 / 35
239.35±0.17	θ_X	15.05±0.17±0.4	12.28±0.07	2289.6 / 35	12.82±0.08	1099.1 / 35
239.35±0.17	θ_Y	14.95±0.16±0.47	12.38±0.08	1701.1 / 35	12.99±0.08	803.0 / 35
p		$\sqrt{\langle\theta^2_{Scatt}\rangle^{meas}_{G4}}$ (mrad)	$\sqrt{\langle\theta^2_{Scatt}\rangle^{true}_{G4}}$	χ^2	$\sqrt{\langle\theta^2_{Scatt}\rangle^{true}_{CC}}$	χ^2
171.9±0.08	θ^2_{Scatt}	29.37±0.61±0.34	71.91±0.59	611929.6 / 43	21.59±0.05	310124.9 / 43
200.11±0.09	θ^2_{Scatt}	25.5±0.38±0.4	41.98±0.11	593015.4 / 43	15.42±0.03	1051864.0 / 43
239.35±0.17	θ^2_{Scatt}	21.09±0.34±0.31	28.29±0.04	466960.1 / 43	6.78±0.01	2167548.3 / 43

6 Results

The residuals between the data and the three models under consideration appear in Fig. 24. The χ^2 derived from these residuals appear in Table 10. The χ^2 was calculated assuming 40 data points so some of the distributions collected show remarkable agreement with data.

The raw and deconvolved data taken with the 200 MeV/c beam are shown in Fig. 25 assuming a GEANT4 LiH simulation. There is very little difference between the GEANT4 simulation, the Carlisle-Cobb simulations and the Moliere calculation, and the deconvolved results are identical.

The fluctuations dominate the processed distribution at angles greater than 45 milliradians for all three data sets as shown in Fig. 17. The distributions of the projections in X and Y were characterized using a Gaussian fit within this range, with the results shown in Table **??** for data and simulation. The table shows that the YZ and XZ projections of the scattering distributions have consistent widths demonstrating that the fiducial selection reduces the asymmetry within the data.

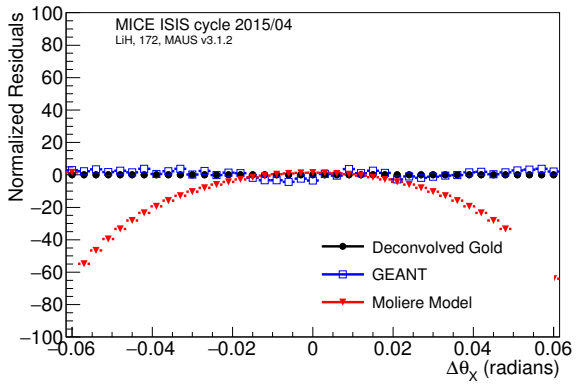

(a) Scattering about X-axis at 172 MeV/c

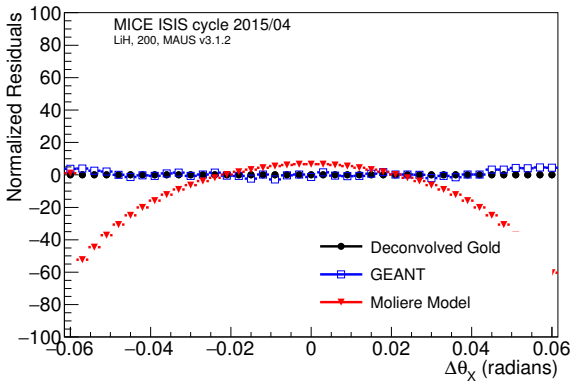

(b) Scattering about X-axis at 200 MeV/c

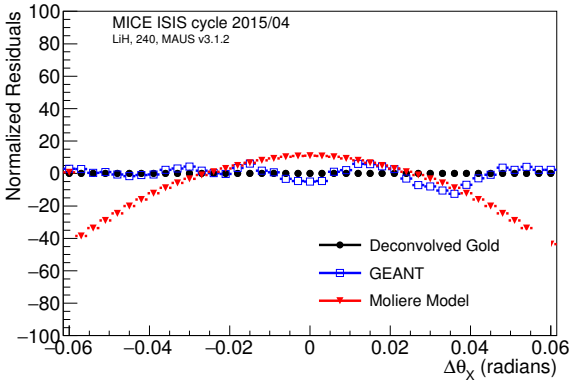

(c) Scattering about X-axis at 240 MeV/c

Figure 24: Scattering residuals between data from a muon beam with the LiH absorber in place compared to three different scattering models in LiH convolved with the scattering data taken without the LiH absorber in place.

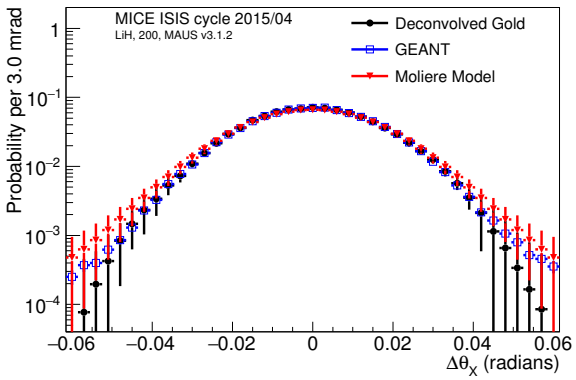

(a) Scattering about X-axis

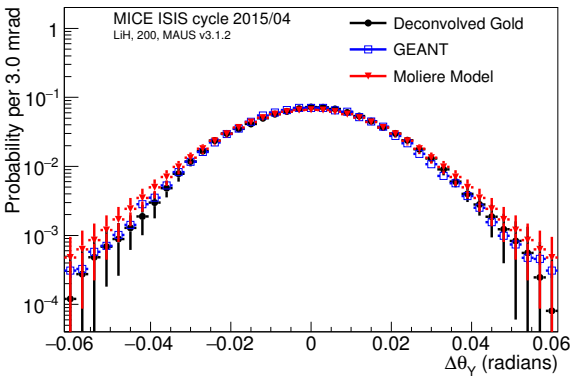

(b) 3D scattering angle

Figure 25: Projected and 3D scattering distributions at 200 MeV/c after deconvolution. The Moliere and Carlisle-Cobb scattering distributions in lithium hydride are provided for comparison.

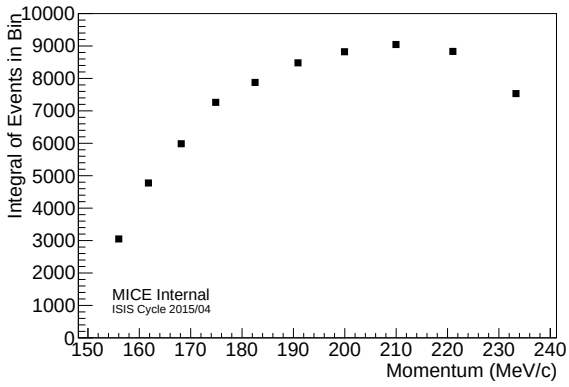

(a) Number of events in TOF bins

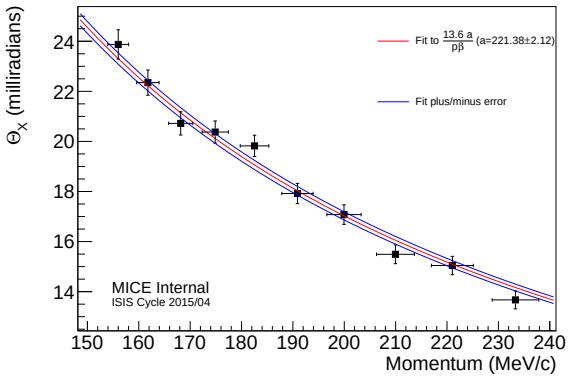

(b) Width in scattering angle $\Delta\theta_X$.

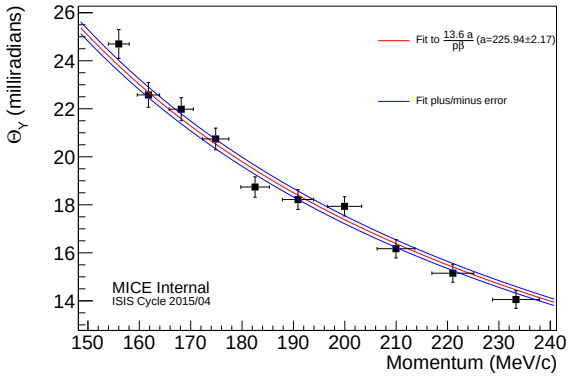

(c) Width in scattering angle $\Delta\theta_Y$

Figure 26: The results of the scattering analysis using data from all three nominal beam settings. Scattering widths are reported after application of deconvolution.

7 Momentum Dependent Measurements

The muon beam data affords a unique opportunity to measure the momentum dependence of the multiple scattering because of the wide momentum distribution. By using the machinery developed to optimize the time of flight selection the widths of the scattering distribution can be determined for each TOF bin, which may be plotted as a function of momentum to confirm the functional representation of the scattering. Each bin is subject to the same analysis as that used to test the nominal scattering momenta. The integral of the events contained in each TOF bin are shown as a function of the mean momentum in Fig. 26a. Only bins with more than 3000 events are used in the analysis. The deconvolved scattering widths as a function of momentum, shown in Fig 26b to **??**, is fit to a $1/p\beta$ dependence motivated by Equation 10. In that case, the coefficient of the momentum dependent term should be 13.6 MeV/c$\sqrt{\frac{z}{X_0}}\left(1+0.038\ln\frac{z}{X_0}\right)$. The offset should be consistent with zero.

The parameters resulting from this fit are shown in Fig. 26 with the upper and lower limits. The values determined from the fits are shown in Table 12. The systematic uncertainty associated with the momentum scale is included in the errors shown in the figures, which were assessed by using the results of the fits with statistical uncertainties only to provide an estimate of the derivative of Θ with respect to momentum and then

Table 11: Measurements of distribution widths and χ^2 between the data after deconvolution of spectra.

p	Angle	Θ^{meas}_{Gold} (mrad)	Θ^{true}_{G4} (mrad)	χ^2	Θ^{true}_{CC} (mrad)	χ^2	$\Theta^{true}_{Moliere}$ (mrad)	χ^2
171.9±0.08	θ_X	19.19±0.22±0.3	18.27±0.16	202.8 / 34	19.96±0.06	585389.6 / 45	20.25±0.46	11055.8 / 45
171.9±0.08	θ_Y	19.04±0.21±0.48	17.97±0.15	359.0 / 34	19.94±0.06	9363781.7 / 180	20.24±0.45	179852.3 / 180
200.11±0.09	θ_X	16.17±0.15±0.4	15.43±0.06	561.1 / 34	16.73±0.05	333203.7 / 45	16.96±0.32	6259.1 / 45
200.11±0.09	θ_Y	16.11±0.15±0.37	15.37±0.06	1114.5 / 34	16.66±0.04	6718669.4 / 180	16.95±0.32	125027.2 / 180
239.35±0.17	θ_X	12.91±0.17±0.34	12.53±0.04	1825.1 / 34	13.67±0.05	116768.6 / 45	13.84±0.25	4229.3 / 45
239.35±0.17	θ_Y	13.11±0.15±0.36	12.56±0.04	1321.5 / 34	13.68±0.05	1583885.3 / 180	13.83±0.25	54983.2 / 180
p		$\sqrt{\langle\theta^2_{Scatt}\rangle^{meas}_{G4}}$ (mrad)	$\sqrt{\langle\theta^2_{Scatt}\rangle^{true}_{G4}}$	χ^2	$\sqrt{\langle\theta^2_{Scatt}\rangle^{true}_{CC}}$	χ^2	$\sqrt{\langle\theta^2_{Scatt}\rangle^{true}_{Moliere}}$	χ^2
171.9±0.08	θ^2_{Scatt}	28.66±0.69±0.35	25.57±0.04	245142.9 / 43	27.79±0.05	32420.3 / 43	28.19±0.05	25893.0 / 43
200.11±0.09	θ^2_{Scatt}	25.45±0.49±0.46	21.68±0.03	244211.9 / 43	23.26±0.03	60206.3 / 43	23.62±0.03	50681.4 / 43
239.35±0.17	θ^2_{Scatt}	21.32±0.5±0.29	17.63±0.02	337249.9 / 43	18.92±0.02	111268.0 / 43	19.31±0.02	80757.3 / 43

to relate the time of flight uncertainty to the momentum i.e.

$$\sigma_\Theta = \frac{d\Theta}{dp}\frac{dp}{dt_{TOF}}\sigma_{TOF} = \frac{\Theta(p + 4\text{ MeV/c}) - \Theta(p - 4\text{ MeV/c})}{8\text{ MeV/c}}\frac{m}{(t_{TOF} - c)^2}\sigma_{TOF} \tag{28}$$

where m and c are provided by the fit to Fig. 10b (m = 835.9±31 ns·MeV/c and $c = 24.01 \pm 0.2$ ns) and $\sigma_{TOF} = 129$ ns as defined for the time of flight systematic. With these errors included in the error bars on the data points the fitted uncertainty (the limits of which are given by the blue lines in the figures) also include the systematic uncertainties.

Measurements using the projected angles are systematically less than the PDG prediction as shown in Fig 26b and Fig 26c. The root mean square scattering angle is consistent with the PDG prediction. The predictions given by GEANT are also shown in the figures, indicating an underestimate of the scattering relative to the PDG formula and the reported data, especially at low momenta. The momentum dependence of GEANT is also not as strong as that of the data.

Table 12: The results of the fit of $a/p\beta$ to the scattering widths as a function of momentum.

Angle	a (mrad)
Θ_X	202.39±6.29
Θ_Y	205.35±6.38
$\sqrt{\langle\theta^2_{Scatt}\rangle/2}$	225±4

8 Conclusion

Presented here is an analysis of the LiH scattering data compiled over ISIS user run 2015/04. These data were compared to different implementations of the multiple scattering in lithium hydride; the compact implementation used as the GEANT default and the full Moliere calculation. A χ^2 statistic was used to make qualitative statements about the validity of the proposed models. The two implementations, when using consistent central momenta, produce consistent results for the LiH disk. A deconvolution procedure was then applied to the data with the same conclusion. Widths from the scattering distributions projected onto the X-Z and Y-Z planes produce consistent results given the uncertainties. These results are larger than the GEANT4 predictions, but smaller than the predictions based on the PDG scattering formula.

The momentum dependence of scattering was examined by considering 200 ps TOF selections from the muon beam data in additions to nominal momenta. This momentum dependence was compared to the dependence in Eq.10 and it was found that the RMS scattering is consistent with the PDG prediction while the widths taken from the projected scattering angles is systematically less than the prediction. Again, GEANT underestimates the scattering at all momenta, although the deviation decreases to be within uncertainties near momenta of 240 MeV/c.

References

[1] **MICE** Collaboration, D. Adams *et al.*, "Characterisation of the muon beams for the Muon Ionisation Cooling Experiment," *Eur. Phys. J.* **C73** no. 10, (2013) 2582, arXiv:1306.1509 [physics.acc-ph].

[2] D. Attwood *et al.*, "The scattering of muons in low Z materials," *Nucl. Instrum. Meth.* **B251** (2006) 41–55, arXiv:hep-ex/0512005 [hep-ex].

[3] **MuScat** Collaboration, W. J. Murray, "Comparison of MuScat data with GEANT4," *Nucl. Phys. Proc. Suppl.* **149** (2005) 99–103. [,99(2005)].

[4] **GEANT4** Collaboration, S. Agostinelli *et al.*, "GEANT4: A Simulation toolkit," *Nucl. Instrum. Meth.* **A506** (2003) 250–303.

[5] L. Urban, "A model for multiple scattering in Geant4,".

[6] **Particle Data Group** Collaboration, K. A. Olive *et al.*, "Review of Particle Physics," *Chin. Phys.* **C38** (2014) 090001.

[7] H. Bichsel, D. E. Groom, and S. R. Klein, "Passage of particles through matter,".

[8] M. Morhac, J. Kliman, V. Matousek, M. Veselsky, and I. Turzo, "Efficient one- and two-dimensional gold deconvolution and its application to γ-ray spectra decomposition," *Nucl. Instr. and Meth. A* **401** no. 2-3, (1997) 385–408.

[9] **MICE** Collaboration, M. Bogomilov *et al.*, "Pion Contamination in the MICE Muon Beam," *JINST* **11** no. 03, (2016) P03001, arXiv:1511.00556 [physics.ins-det].

[10] R. M. Gray, "Toeplitz and circulant matrices: A review," *Foundations and Trends in Communications and Information Theory* **2** no. 3, (2006) 155–239. http://dx.doi.org/10.1561/0100000006.

A Gold's Deconvolution Algorithm

The scattering distribution that is measured by MICE can be stated as:

$$x'(\theta) = \int_{-\infty}^{t} x(\Theta)h(\theta - \Theta)d\Theta + n(\theta) = x(\theta) * h(\theta) + n(\theta), \tag{29}$$

where $x'(t)$ is the scattering distribution measured with the absorber in the channel including scattering contributions from interstitial material in the channel and the resolution of the tracker. $h(t)$ is the scattering distribution measured with the absorber removed but still including the interstitial material and the tracker resolution. $x(t)$ is the scattering distribution due only to the absorber material without the interstitial material in the channel and without the tracker resolution. $n(t)$ is additive noise and the $*$ denotes the convolution operator. For discrete systems, this statement can be expressed as:

$$x'(i) = \sum_{k=0}^{i} x(k)h(i-k) + n(i) = x(i) * h(i) + n(i), \tag{30}$$

an expression which represents a general system of linear equations that can be written in matrix form as:

$$x' = Hx + n \tag{31}$$

where the matrix H has dimension $N \times M$, the vectors x' and n have N elements and the vector x has M elements, while $N \geq M$. To find a least squares solution of the system of linear equations given in 31

$$||Hx - x'||^2 \tag{32}$$

must be minimised. Several methods have been developed that regularise the output and prevent large fluctuations entering the solution. One such method is the Gold algorithm. Starting from the expression:

$$x' = H'x \tag{33}$$

where $H' = H^{\boldsymbol{T}}HH^{\boldsymbol{T}}$ and $H^{\boldsymbol{T}}$ is a Toeplitz matrix[1]. x' is known from data, and the method iterates over:

$$x_i^{(k+1)} = \frac{x'_i}{\sum_{m=0}^{N-1} H'_{im}x_m^{(k)}} x_i(K) \tag{34}$$

where

$$\begin{aligned} i &= 0, 1, ..., N-1, \\ k &= 1, 2, 3, ..., L, \\ x^0 &= [1, 1..., 1]^T \end{aligned} \tag{35}$$

and where L is the number of iterations. The method also incorporates a boosted deconvolution technique whereby for each iteration if the repetition number, R, is greater than r which is initially defined to be one then

$$x^{(0)}(i) = [x^{(L)}(i)]^p \tag{36}$$

where p is the boosting coefficient and r now becomes $r = r + 1$ whereafter the deconvolution continues. In this particular case $r = 0$. This method is encapsulated in a ROOT class TSpectrum [8] and was used to treat the data as an unfolding step. Data were taken both with and without the absorber in the channel as summarised

[1] A Toeplitz matrix is an $n \times n$ matrix $T_n = [t_{k,j}; k, j = 0, 1, ..., n-1]$ where $t_{k,j} = t_{k-j}$ [10]

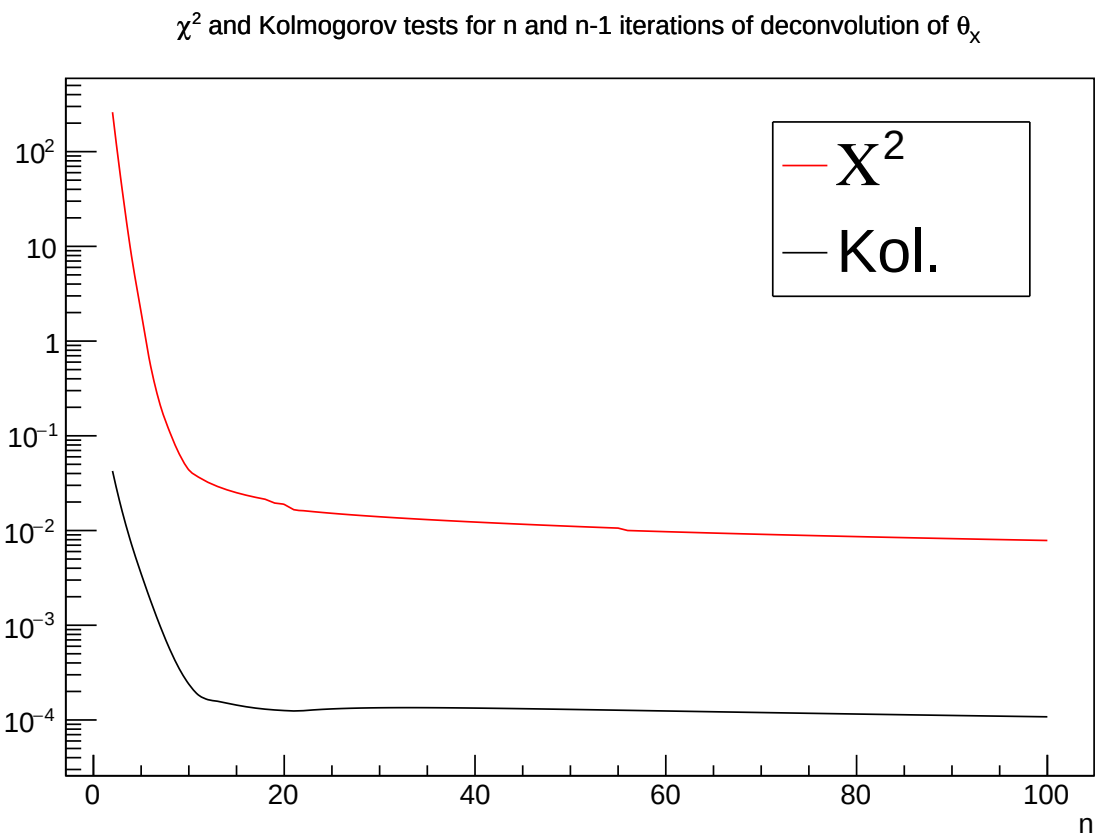

Figure 27: The convergence plot for the 204 M/c θ_x scattering deconvolution distribution.

in table 2a. The ROOT class accepts histograms as input and the scattering distributions for the two cases, with and without absorber, were used as input with the output being the final measured scattering distribution. The algorithim typically converged to a solution after $\sim$ 10 iterations with an example convergence plot shown in figure 27.